TECHNISCHE UNIVERSITÄT WIEN

DIPLOMARBEIT

Numerical Simulation of Core-Level Spectroscopies

Ausgeführt am
Institut für Festkörperphysik
der Technischen Universität Wien

unter der Anleitung von:
Associate Prof. Dr. Jan Kuneš
und:
Dr. Atsushi Hariki

durch

Mathias Winder, BSc
Matrikelnummer: 01230412

Wien, 25. Juni 2018

_____
(Unterschrift Verfasser/in)

_____
(Unterschrift Betreuer/in)

1 Abstract

Core-level X-ray spectroscopies are widely used for investigating electronic structures of transition metal (TM) compounds. In core-level spectroscopies an incident photon excites a core electron where the created core hole acts as a positive test charge. The electronic properties can be determined by core-level spectra, influenced by the reaction of the system to the core hole.

For the investigation of TM compounds different kinds of core-level X-ray spectroscopies are available. X-ray photoemission spectroscopy (XPS) provides photoelectron spectra, whereas X-ray absorption spectroscopy (XAS) provides absorption spectra due to the excitation of core electrons to valence states. Resonant inelastic X-ray scattering (RIXS) is a second-order optical process where the incident photon gets absorbed, such as in XAS, but the spectra are generated by relaxation processes.

We present within this thesis a computational study of Cu L-edge RIXS for $LaCuO_3$ and $NaCuO_2$ which are two typical high-valence transition-metal oxides. Basis of the approach is a theoretical framework based on the local-density approximation and dynamical mean-field theory (LDA+DMFT) which is applied on the Anderson impurity model (AIM) to calculate spectral functions of various core-level X-ray spectroscopies. Recent experiments revealed unusual coexistence of bound and continuum excitations in the L-edge RIXS spectra where the underlying physics is still a challenging part of research. This study is motivated by these experiments and we analyze in detail the behavior of the fluorescence-like (FL) feature and show how it is connected to the details of the electronic and crystal structure. On the studied compounds we demonstrate how material details determine whether the electron-hole continuum can be excited in the L-edge RIXS process.

Contents

2 Introduction

2.1 Transition Metal Oxides

Transition metal (TM) compounds exhibit a broad spectrum of functionalities, such as high-temperature superconductivity T_c, colossal magneto-resistance or ferro-electricity, and have been attracting much attention in the recent years [1, 2, 3]. TM compounds show phase transitions between distinct thermodynamic phases with dramatically different electronic and magnetic properties. These properties are intriguing for the application as well as for fundamental science. Thus a microscopic understanding of the electronic structure of TM compounds has been one of the central topics in modern solid state physics.

Transition metal oxides (TMO) belong to a distinct category, *strongly correlated materials*, where nontrivial electronic correlation due to the interplay of the itinerancy of electrons and the Coulomb interaction gives rise to a qualitatively different low-energy physics. A theoretical description of the electronic structure in the strongly correlated material is challenging since the importance of electronic correlation requires a many-body treatment of the electronic system. For example, static Hartree-Fock mean-field theory or a simplified band calculation based on density functional theory (DFT) fail in explaining even fundamental properties of TM compounds, such as the insulating character of NiO with a sizable charge gap ($\sim$4 eV) [4, 5, 6, 7].

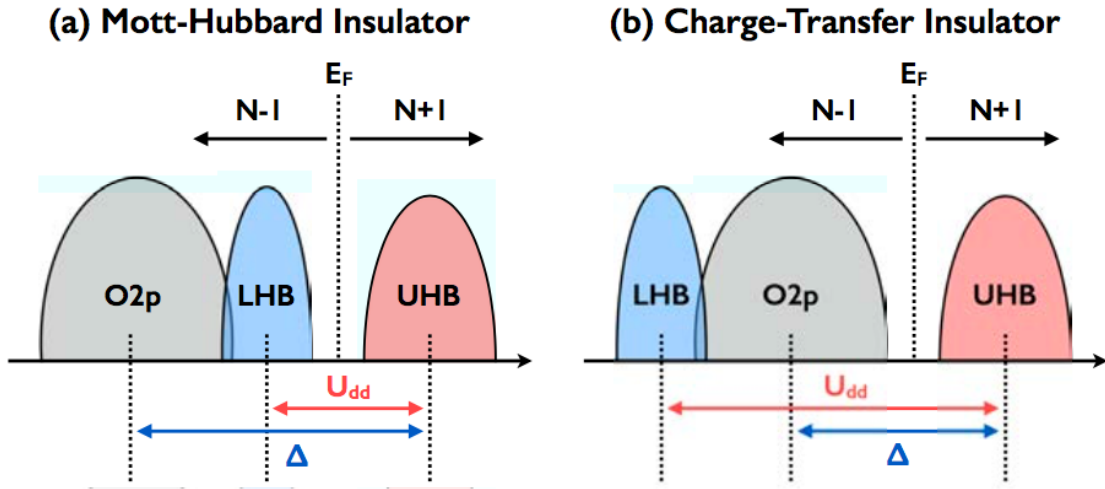Figure 1: (a) Mott Insulator: the upper (lower) Hubbard band lies above (below) the Fermi-level E_F, the oxygen $2p$ states lie below the lower Hubbard band (b) Charge-Transfer Insulator: the O $2p$ states lie above the lower Hubbard band but below the Fermi-level; adapted from [8] with the permission from the author

The Hubbard model is a paradigm model describing the correlated physics in TM

systems, which takes into account the electron hopping between the different TM sites and the on-site Coulomb repulsion between the electrons. The Hubbard model describes the metal-insulator transition driven by purely electronic correlation, the so-called "Mott transition" [9]. The Mott insulator is distinct from other uncorrelated insulators, such as the band insulator or Slater insulator, which can be described by one-particle theories, for example Hartree-Fock theory or DFT. In the Mott insulator, the gap opens when the energy gain due to the electron hopping ($\sim t$) becomes smaller than the energy loss due to the electronic repulsion acting between electrons sitting on the same TM site ($\sim U_{dd}$) in the charge fluctuation: $d_i^n d_j^n \rightarrow d_i^{n-1} d_j^{n+1}$, where i,j denote the position of TMs. In the Mott insulator, the TM $3d$ band splits into the so-called lower Hubbard band (LHB), formally part of the valence band, and upper Hubbard band (UHB), formally part of the conduction band, see Fig. 1.

In real TM compounds the hopping process can be more complicate and involve also ligand atoms. The TM d-orbitals usually overlap with the ligand orbitals. Therefore electrons from the occupied ligand states, e.g. oxygen $2p$, can be transferred to the TM ion, described as $d_{TM}^n p_O^i \rightarrow d_{TM}^{n+1} p_O^{i-1}$, which costs the charge transfer energy Δ. When the charge transfer energy Δ is smaller than the on-site Coulomb repulsion U_{dd}, the ligand $2p$ states are on top of the valence band, which is called charge transfer insulator [10], see Fig. 1(b).

TM compounds with high valence states can have a small or negative charge transfer energy Δ, implying an overlap between the UHB and the ligand band. The resulting state can be metallic with a large contribution of oxygen states at the Fermi level. An interesting phenomenon found in some high valence TM compounds is a spontaneous charge disproportionation. For example in $NdNiO_3$ where states with Ni^{3+} decompose into Ni^{2+} and Ni^{4+}. The real electronic structure is more likely Ni^{2+} and $Ni^{2+}\underline{L}^2$ with quantum numbers ($S = \frac{8}{2}$ and $S = \frac{6}{2}$, respectively) due to the instability of Ni^{3+} or Ni^{4+}. The process is schematically captured by [11, 3]

$$2Ni^{2+}\underline{L} \rightarrow Ni^{2+} + Ni^{2+}\underline{L}^2, \tag{1}$$
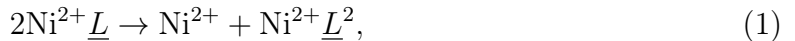
where $\underline{L}$ denotes a hole in the ligand $2p$ state. One nickel atom remains in the Ni^{2+} state and forms ionic bonds, whereas the other Ni atom forms covalent bonds with the oxygen ligands. The bond length of the covalent bonds is shorter than the bond length of the ionic bonds of the Ni^{2+} ions. The disproportionation of the Ni-O bonds leads to a structural deformation of the crystal.

2.2 Core-Level X-ray Spectroscopy

Core-level X-ray spectroscopy is a powerful tool to study the electronic structure in strongly correlated system including $3d$ TM materials. An incident photon excites an electron from a core state in the material. The core hole created by the incident photon, which acts as a positive test charge, is generally well localized and thus interacts strongly with the valence electrons with a localized wave function. Therefore the core-level spectra provides information on electronic properties of the strongly correlated system. Though

the core-level X-ray spectroscopy has been widely applied in the study of TM systems since early 1970's, recent experimental developments, especially in energy resolution and bulk sensitivity, have opened new opportunities to study fine electronic features which are related directly to emergent low-energy physics. Thus a further development of theoretical method to analyze spectral fine features is desired. Since the present thesis contributes to this direction, we review below experimental and theoretical aspects of core-level X-ray spectroscopy below [12, 13, 8].

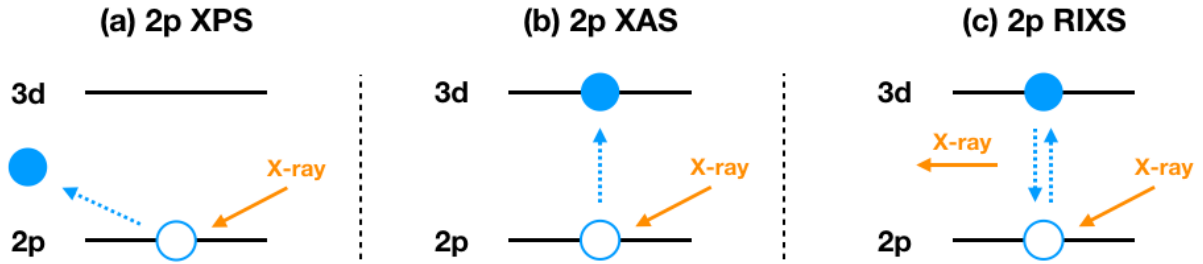### 2.2.1 Experimental Aspects of Core-Level X-ray Spectroscopy

Figure 2: Schematic pictures of $2p$ core-level excitation processes: (a) X-ray photoemission (XPS), (b) X-ray absorption spectroscopy (XAS), and (c) $2p$-$3d$ resonant inelastic X-ray scattering (RIXS); adapted from [8] with the permission from the author

Fig. 2 shows $2p$ core-level excitation processes, which are typically employed in the study of $3d$ TMO [12, 13]. The different excitation processes have different selection rules and final states. Thus a combination of different excitation processes enables us to study details of the material of interest. For example, in $2p$ X-ray photoemission spectroscopy (XPS), see Fig. 2(a), a $2p$ core electron is emitted from the system by the incident photon. The $2p$ core hole left in the material breaks the charge neutrality locally. This induces a strong charge response from valence electrons on surrounding atoms, which is traditionally called charge-transfer (CT) screening. The $2p$ XPS spectra reflect the valence structure through the CT screening [12]. In contrast, $2p$ X-ray absorption spectra (XAS) conserves the charge neutrality and the $2p$ core hole in the final states is effectively screened by the excited electron largely remaining on the excited TM site, see Fig. 2(b). Thus $2p$ XAS is known to be useful to study the atomic-multiplet structure on a specific TM atom [14]. However, a sensitivity of $2p$ XAS fine features to nonlocal effects is speculated about recently [15, 16]. The nonlocal effects in $2p$ XAS are theoretically investigated in this thesis. The $2p$-$3d$ resonant inelastic X-ray scattering (RIXS), see Fig. 2(c), is a coherent second-order optical process, that has been

attracting attention due to a dramatic improvement of the energy resolution in recent years [17, 18, 19]. The incident X-rays is absorbed in a $2p \rightarrow 3d$ process, and subsequently, a valence $3d$ electron decays into the $2p$ core hole with X-ray emission. The energy loss $\omega_{\text{loss}} = \omega_{\text{out}} - \omega_{\text{in}}$ probes the low-energy excitations of the target system. Thanks to the broad sensitivity of RIXS to charge, spin and orbital degrees of freedoms, the spectra show various two-particle excitations of the system, ranging from CT excitations ($5 \sim 10$ eV), atomic multiplet excitations ($\sim$ a few eV) often called d–d excitations, and low-energy elementary excitations, such as magnons ($\sim$ a few 100 meV) or phonons ($\sim$ a few 10 meV), see Fig. 13. Thus RIXS is becoming widely applied to the study of correlated electron systems. We mention that intensities of RIXS spectral features generally show a clear dependence on the incident photon energy ω_{in}, indicating that the understanding of the character of the intermediate states is important to interpret the RIXS features properly [15, 20, 21].

2.2.2 Theory of Core-level X-ray Spectroscopy

Theoretical analysis of the experimental spectra is a crucial step to extract electronic information hidden in the spectra. We review here the theoretical description of core-level X-ray spectroscopies and introduce the single impurity-model approach, which is widely employed in the analysis of various core-level spectra. Then we describe recent developments in theoretical description using local density approximation (LDA) and dynamical mean-field theory (DMFT), introduced to analyze spectral fine features in $2p$ XPS for TMO [22].

First we review the theoretical description of the spectral functions of $2p$ XPS, $2p$ XAS and $2p$-$3d$ RIXS in $3d$ TMO. The spectral function of $2p$ XPS is given by Fermi's golden rule [12]

$$F_{\text{XPS}}(\omega_k) = \sum_f \left| \langle f | \hat{T}_{\text{D}} | g \rangle \right|^2 \delta(E_g + \hbar\omega_k - E_f), \qquad (2)$$

where $|g\rangle$ and $|f\rangle$ are the ground and final states, respectively. Note that $|f\rangle$ is the eigenstate of the electronic system with an extra $2p$ core hole. E_g, E_f, and ω_k denote the energy of the ground state, final state and the photoelectron emitted from the system. The delta function represents the energy conservation in the XPS process. The photoelectron is assumed to propagate at a plane wave, which is a reasonable assumption in the high-energy X-ray regime. The dipole operator $\hat{T}_{\text{D}}$ creates a $2p$ core hole and the photoelectron. Similarly the spectral function of $2p$ XAS is given by

$$F_{\text{XAS}}(\omega_k) = \sum_f \left| \langle f | \hat{T}_{\text{D}} | g \rangle \right|^2 \delta(E_g + \hbar\omega_k - E_f). \qquad (3)$$

Here ω_k denotes the energy of incident photon. The photon excites a $2p$ core electron to an empty state in TM $3d$ shell. $\hat{T}_{\text{D}}$ represents the dipole transition. We point out that the final state $|f\rangle$ is the eigenstate of the electronic system with an extra $2p$ core hole and an extra valence electron, which differs from that in the $2p$ XPS. The spectral

function of 2p-3d RIXS is given by the Kramers-Heisenberg formula [?]

$$F_{\mathrm{RIXS}}(\omega_{\mathrm{in}}, \omega_{\mathrm{out}}) = \sum_f \left| \sum_m \frac{\langle f|\hat{T}_{\mathrm{E}}|m\rangle \langle m|\hat{T}_{\mathrm{I}}|g\rangle}{\hbar\omega_{\mathrm{in}} + E_g - E_m + i\Gamma_{\mathrm{L}}} \right|^2 \delta(\hbar\omega_{\mathrm{in}} + E_g - \hbar\omega_{\mathrm{out}} - E_f), \quad (4)$$

where $|g\rangle$, $|m\rangle$ and $|f\rangle$ are the ground, intermediate and final states, respectively. The intermediate state $|m\rangle$ has a 2p core hole and an extra valence electron, induced by the dipole transition operator $\hat{T}_{\mathrm{I}}$, while $|f\rangle$ has the same core configurations as the initial state since $\hat{T}_{\mathrm{E}}$ fills the core state by emitting a photon with the energy ω_{out}. Thus the eigenspectra of the subspaces containing $|m\rangle$ and $|f\rangle$ are identical to those of the final and ground state in the 2p XAS, respectively. Γ_{L} represents the life-time broadening of the 2p core hole.

The computation of the spectral function in the infinite electron system is a demanding task. Since the core hole created by the incident photon is well localized, the atomic model gives a good starting point for the theoretical modeling of core-level X-ray spectra. The atomic model is known to give a reasonable description of the 2p XAS in 3d TMO [12, 14] since the XAS spectrum, that conserves the charge neutrality, is usually dominated by the atomic multiplets. However, in 2p XPS, the atomic model fails even in providing global spectral features, since the CT screening from surrounding valence electrons driven by the core-hole creation at the excited TM site affects the spectral shape substantially. A cluster model was introduced to take into account CT from nearest-neighbor ligands in 1980's, see Fig 3. Despite a great success of the cluster model in providing the fundamental spectral interpretation [12, 23, 24], recent high-resolution and bulk-sensitive experiments exposed the oversimplification in the cluster model description [25, 26]. To overcome the problems in the cluster-model description, a new approach is proposed recently, which is based on local-density approximation (LDA) and the dynamical mean-field theory (DMFT). In this approach the Anderson impurity model with a continuous bath is used to compute the core-level spectra. The success of the approach stands on the use of the continuous bath states obtained from the LDA+DMFT calculation. Thus, for example, the CT effect due to a long-distant hopping can be described by the Anderson impurity model properly. In addition, the ambiguity of the model with many parameters is removed by the (almost) parameter-free description of LDA+DMFT. We briefly describe the cluster model and the LDA+DMFT approach below [8].
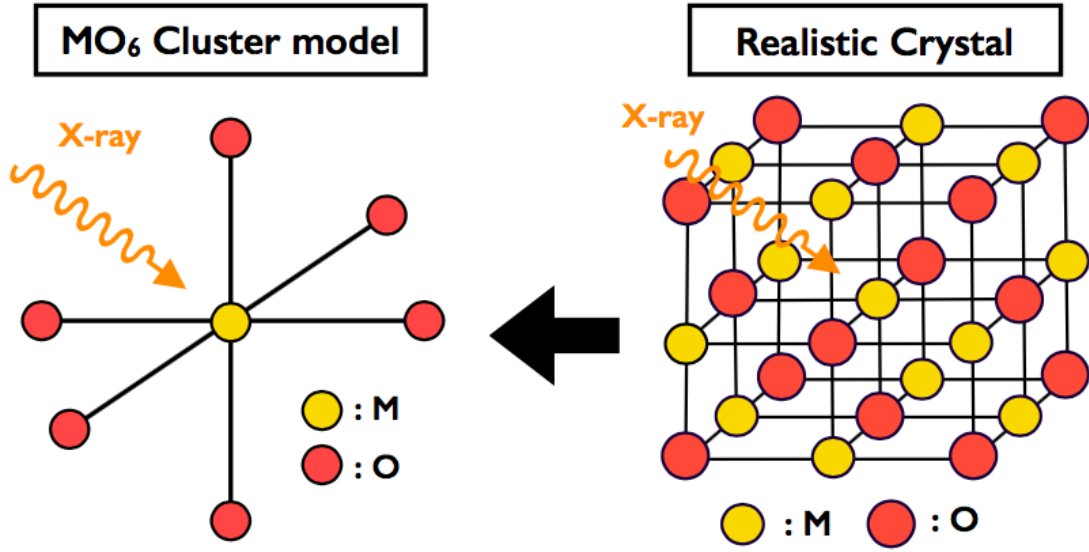
Figure 3: The MO_6 cluster model takes into account excited TM ion and nearest-neighboring ligands; adapted from [8] with the permission from the author.

Cluster Model: The cluster model achieved a remarkable success in the Ni $2p$ XPS analysis of NiX_2 (X=F, Cl, Br) by Okada et al. [23], and then, it has been widely employed in spectral analysis of various types of core-level spectra for strongly correlated materials [12, 24]. The MO_6 cluster model consists of a TM ion and the nearest-neighbor oxygen ligands, see Fig. 3. For the $2p$ core-level excitation in $3d$ TMO, TM $3d$, $2p$ core and oxygen $2p$ states are considered explicitly. The Hamiltonian of the cluster model includes following terms: the atomic Coulomb multiplet interaction between TM $3d$ electrons, and that between $3d$ electrons and $2p$ core hole; crystal field splitting; hybridization of TM $3d$ and O $2p$ states. The explicit form of the Hamiltonian is given in Ch. 3.4.1. The interaction terms are represented by so-called solid parameters: Δ, $10Dq$, $V_{pd}(e_g), V_{pd}(t_{2g}), U_{dd}$ and U_{dc}. In the cluster-model analysis, the solid parameters are fixed by fitting the experimental spectra. The CT energy Δ measures the energy cost of an electron transfer from the ligand $2p$ state to TM $3d$ state. In the crystal, the five-fold degeneracy of the $3d$ states in spherical symmetry is removed by the static electric field produced by the ligands, the so-called crystal field splitting. In the octahedral symmetry (O_h), the $3d$ energy levels split into doubly-degenerate e_g states and triply-degenerate t_{2g} states. The $10Dq$ parameter defines the size of the crystal-field splitting. $V_{pd}(e_g)$ ($V_{pd}(t_{2g})$) represents the hybridization intensity of the e_g (t_{2g}) state with O $2p$ states. The U_{dd} (U_{dc}) is the value of the monopole part of the Coulomb interaction between $3d$ electrons (between $3d$ electrons and the TM $2p$ core hole). The core-valence interaction is attractive, and thus the energy levels of $3d$ states are effectively lowered by the presence of the core hole, which induces the CT screening from neighboring ligands.

Fig. 4 shows the Ni $2p$ XPS spectrum in NiO calculated by the cluster model (right)

9

and recent experimental data (left) [26]. We see the $2p_{3/2}$ (853~869 eV) and $2p_{1/2}$ (870~886 eV) components, which are split due to the spin-orbit interaction in the Ni $2p$ core states. In both components, the CT satellites (~860 eV for $2p_{3/2}$ and ~880 eV for $2p_{1/2}$) and the main-line (ML) structures (~856 eV for $2p_{3/2}$ and ~872 eV for $2p_{1/2}$) are observed. We point out here that the $2p_{3/2}$ ML shows double peaks marked A and B. Though the cluster-model calculation well reproduces the global $2p$ XPS structures, the double-peak structure in the ML is missing in the calculated spectrum. The $2p$ XPS ML is sensitive to the CT screening in the final state. Thus the failure of the cluster model suggests the importance of the CT with a long-distance hopping, traditionally called the non-local screening, such as due to the CT between different TM sites. Following Hariki [8], similar fine spectral features due to the non-local screening have been observed in many $3d$ TMO, such as vanadates [27, 28, 29, 30, 31], manganites [32, 33, 34, 35], chromates [36], titanates [37], magnetites [38], nickelates [39] and high-T_c cuprates [25], where a close relation of these features to low-energy physics is speculated. Thus a further development of theoretical approaches to overcome the limitation of the cluster model is desired.
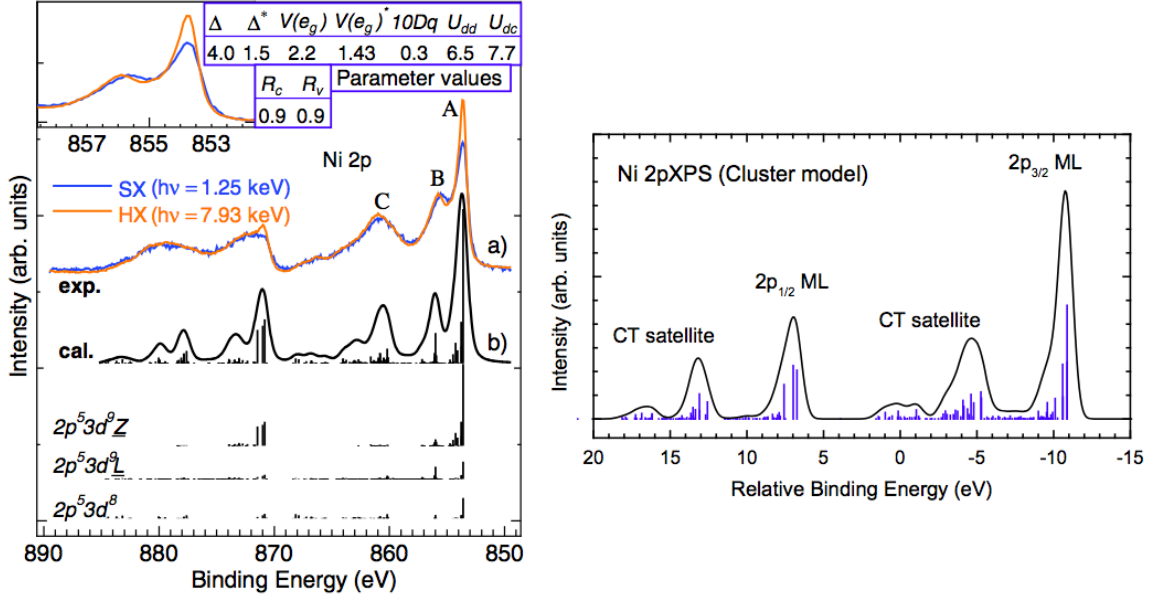

Figure 4: (left) Experimental data of Ni $2p$ XPS in NiO [26]. (right) Calculated spectrum by the NiO$_6$ cluster model XPS [8].

Anderson impurity model: Anderson impurity model (AIM) was introduced by P. W. Anderson in his study of "localized magnetic states in metals" in 1961 [40]. The AIM describes a TM ion embedded in continuum of metallic states (bath). It is known that the IAM captures various phenomena emerging from interaction between the localized and itinerant electrons, such as the Kondo effect [3]. The AIM was applied to core level X-ray spectroscopy for La metal by Kotani and Toyozawa in 1974 [41] and for

Ce compounds by Gunnarsson and Schönhammer in 1983 [42]. The AIM takes into account the continuous bath representing the electronic bands in infinite crystal instead of discrete ligand states as in the cluster model, see Fig. 5. Thus the CT effect due to a long-distant hopping can be described by the IAM. However, difficulties come in the construction of the bath that takes into account the electronic correlation properly, which has lead to a practical use of a simplified model density of states (DOS), such as rectangular or semi-elliptical form. Indeed it is known that the fine spectral features revealed in $2p$ XPS can be reproduced with the use of the simplified DOS [43, 25]. The details of the AIM is given in Ch. 3.4.1.
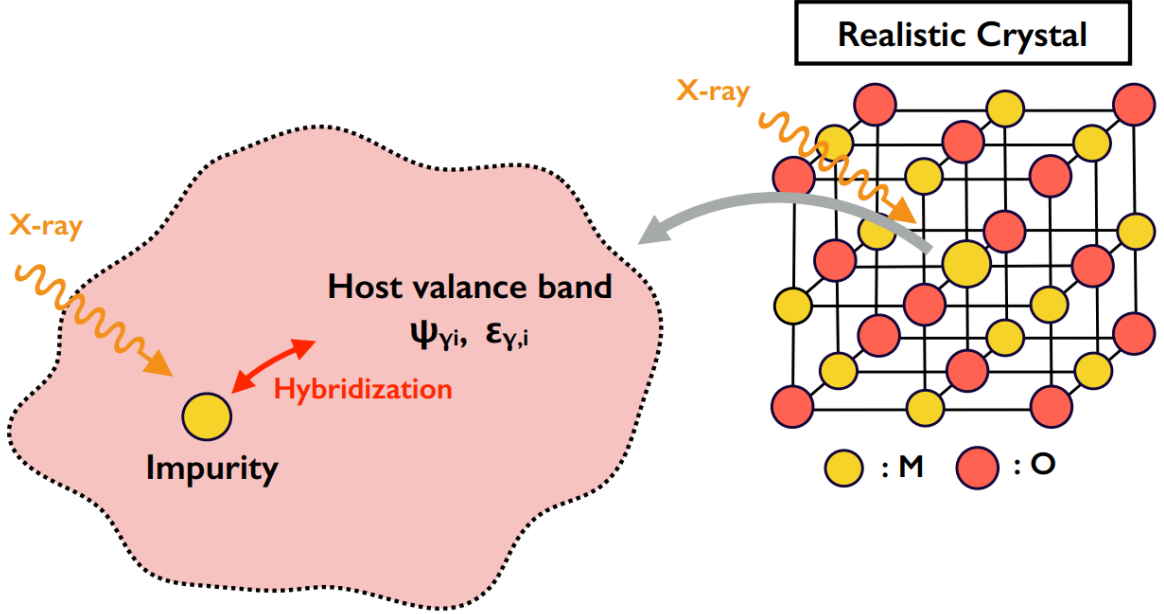

Figure 5: AIM with the host valence band as bath states

Anderson impurity model with LDA+DMFT: A new theoretical method was proposed recently to analyze fine spectral features in $2p$ XPS of TMO. The approach is based on local density approximation (LDA) + dynamical mean field theory (DMFT). The heart of this approach is the use of the continuous bath states obtained from LDA+DMFT for the core-level spectroscopy calculation. The LDA+DMFT is a modern *ab*-initio many-body scheme and is capable to capture various types of electronic properties in materials with strongly correlated electrons [44, 45, 46]. For example, LDA+DMFT gives the insulating solution with the sizable gap (~ 4 eV) for NiO in agreement with experiments [4, 5, 6]. The LDA+DMFT calculation proceeds in the two steps: (1) construction of an effective dp model from a converged LDA calculation and (2) solution of the DMFT equations to include correlation effect in lattice. The effective Hamiltonian takes into account the electronic bands around the Fermi energy level, usually TM $3d$ and O $2p$ bands in TM compounds, often called dp model. In practice the effective model is obtained by constructing the localized Wannier functions

from the target bands [47, 48]. Then the effective model is solved within the DMFT approximation that takes into account the energy dependence in the self-energy but neglects its momentum dependence. The self-energy describes the local electron dynamics due to the strong electronic interaction between $3d$ electrons and renormalizes the bare electronic bands. In the new approach, the core-level spectra are calculated by the AIM with the continuum bath states obtained by LDA+DMFT. The AIM is augmented by the $2p$ core state. The AIM describes the hopping between the excited TM ion (impurity) and the whole valence bands with electronic correlation. Hariki et al. [22] applied the new approach to a systematic analysis of $2p$ XPS in TMO and found a quantitative agreement with recent high-resolution experiments including the fine spectral features originating from the nonlocal screening [49].

2.3 Motivation

Recent experimental progresses in core-level X-ray spectroscopy have opened new opportunities to study in detail electronic properties in strongly correlated systems including $3d$ TMO. To catch up with the experimental development, new theoretical approach based on LDA+DMFT has been proposed recently [22]. The LDA+DMFT approach has following advantages to the conventional cluster model: (1) elimination of the ambiguity in the parameter choice by almost parameter LDA+DMFT scheme. (2) accurate description of the CT effect not only from neighboring ligand states but also from the correlated $3d$ bands enabled by replacing the discrete ligand states by ab-initio (LDA+DMFT) continuous bath representing the crystal environment of the excited atom.

The ability for a detailed "fine-feature" analysis in core-level XPS with the LDA+DMFT approach is demonstrated recently by Hariki et al [22]. However the capability of the LDA+DMFT approach to describe other core-level excitation processes is a open question. For example, it is widely accepted that the cluster model or the atomic model gives a reasonable description of the $2p$ XAS in $3d$ TMO since the core hole is already screened by the excited electron in the on-site TM $3d$ shell effectively. The quantitative description of $2p$ XAS and moreover of $2p$-$3d$ RIXS spectra with the LDA+DMFT approach has to be verified by comparison with experimental studies and requires a further development on the computational side.

In this thesis, we apply the LDA+DMFT approach to the analysis of $2p$ XAS and $2p$-$3d$ RIXS for the first time [15]. We study Cu L-edge for the two isoelectric cuprates; $LaCuO_3$ and $NaCuO_2$. By a direct comparison of results by the cluster model and LDA+DMFT approach, we reveal the importance of the nonlocal effect in Cu $2p$ XAS for high-valence cuprates. Besides we develop the computational method for computing $2p$-$3d$ RIXS, which includes the intermediate state and the electron-hole pair creation in LDA+DMFT continuous bath properly. With this development, we study the mechanism of the fluorescence-like behavior and its coexistence with the Raman-like feature in $2p$-$3d$ RIXS spectra, which is under active debate [21, 20]. Based on the LDA+DMFT results we discuss the material-specific nature of the fluorescence-like feature.

3 Theory

In this chapter, we describe our theoretical approach for calculating core-level spectra the using LDA+DMFT scheme. The calculation proceeds in three steps: (i) construction of a dp model from the converged LDA calculation, (ii) solution of the DMFT self-consistent equation for the dp model to obtain the DMFT hybridization function, and (iii) calculation of the core-level spectra using the extended Anderson impurity model (AIM) with the DMFT hybridization function.
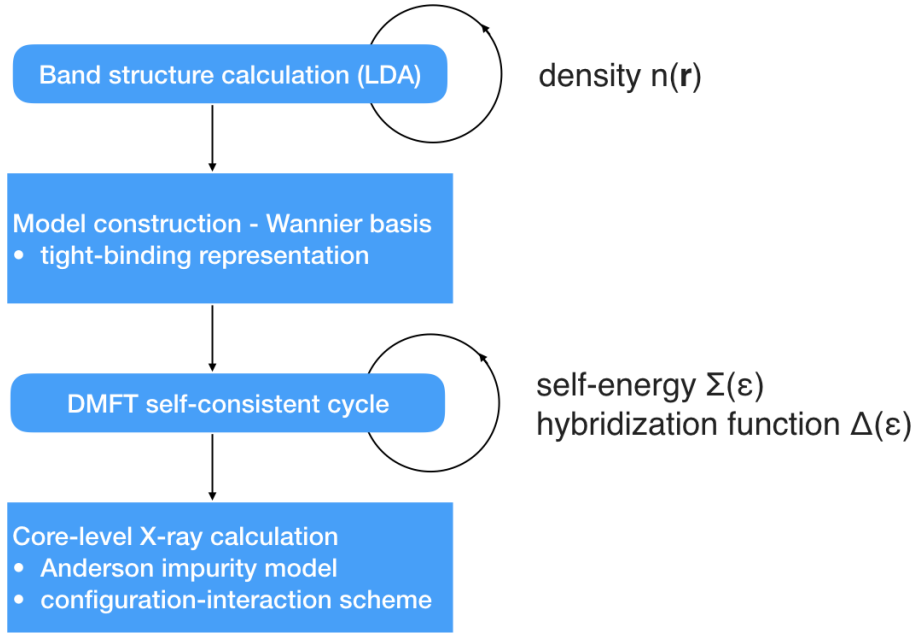

Figure 6: Flow chart of LDA+DMFT AIM Calculation

Figure 6 summarizes the computational steps. Steps (i) and (ii) are standard for the LDA+DMFT method. Starting with the converged LDA calculation for the crystal structure determined experimentally, the dp model is constructed via the Wannier projection. The dp model, which takes into account TM $3d$ bands and O $2p$ bands, can describe physically-important low-energy excitations as well as high-energy excitations inevitably involved in core-level excitation processes. The dp model, including the Coulomb interaction between $3d$ electrons, is solved within the DMFT approximation. The heart of the method is the mapping of the lattice problem onto the AIM with a self-consistently determined DMFT hybridization function $\Delta(\omega)$. The valence bands in the whole lattice is effectively represented by a continuous function $\Delta(\omega)$. Thus the AIM can describe the charge transfer (CT) effect not only from neighbor ligands but also other TM $3d$ ions. The AIM is then augmented with TM $2p$ core states. The core-level spectra are calculated by using the configuration-interaction scheme, which enables us to compute spectral functions directly along the real-frequency axis without losing information on fine band features in $\Delta(\omega)$ and the multiplet structures due to the

$2p$-$3d$ Coulomb interaction. The details of each step are given below. References on the LDA+DMFT and core-level spectroscopy are found in Refs. [12, 50, 3]

3.1 Density Functional Theory

Density functional theory (DFT) allows to describe some aspects of the many-body problem for real materials with low computational costs. Hohenberg and Kohn [51] and Kohn and Sham [52] showed, that the non-degenerate ground state of the N-electron Schrödinger equation is determined uniquely by the electron density. The two main statements of Hohenberg-Kohn theorem [51] are:

- There is a one to one mapping between an external potential $V(\boldsymbol{r})$ and the ground state particle density $n(\boldsymbol{r})$.

- The ground state of a system characterized by the external potential $V(\boldsymbol{r})$ can be obtained by the minimization of a functional $E[n(\boldsymbol{r})]$.

The ground state energy can then be determined by the variational principle:

$$\frac{\partial E[n(\boldsymbol{r})]}{\partial n(\boldsymbol{r})}\bigg|_{n(\boldsymbol{r})=n_0(\boldsymbol{r})} = 0 \tag{5}$$

There are various approximations within DFT. We review in the following the local density approximation (LDA).

3.1.1 Local Density Approximation

The minimization of the functional can be achieved through a self-consistent solution of one-particle Kohn-Sham equations. The Kohn-Sham and Hohenberg-Kohn theorems show, that the energy $E[n(\boldsymbol{r})] = F[n(\boldsymbol{r})] + \int n(\boldsymbol{r})V(\boldsymbol{r})d^3r$ can be written as a functional of the particle density $n(\boldsymbol{r})$ with an external potential $V(\boldsymbol{r})$. We use the ansatz $n(\boldsymbol{r}) = \sum_i f_i |\Psi_i(\boldsymbol{r})|^2$ with the constrains of the particle number conservation $N = \int n(\boldsymbol{r})d^3r$ and the mutual orthogonality of the one-particle wave functions $\Psi_i(\boldsymbol{r})$. The external potential can be for example the Coulomb interaction between the protons in the core and the electrons. The energy functional has the following form

$$E[n(\boldsymbol{r})] = \underbrace{T[n(\boldsymbol{r})] + \frac{e^2}{2} \int \int \frac{n(\boldsymbol{r})n(\boldsymbol{r}')}{|\boldsymbol{r} - \boldsymbol{r}'|} d^3r d^3r' + E^{xc}[n(\boldsymbol{r})]}_{F[n(\boldsymbol{r})]} + \int n(\boldsymbol{r})V(\boldsymbol{r})d^3r, \tag{6}$$

where $T[n(\boldsymbol{r})]$ is the kinetic energy of the non-interacting particles. The second term in Eq. 6 is the Hartree energy which describes the electrostatic interaction of the electrons. The exchange and correlation functional $E^{xc}[n(\boldsymbol{r})]$ includes the exchange energy ε_{xc} of one particle in an electronic gas

$$E^{xc}[n(\boldsymbol{r})] = \int n(\boldsymbol{r})\varepsilon_{xc}[n(\boldsymbol{r})]d^3r. \tag{7}$$

There are several possibilities to approximate ε_{xc}, for example the local density approximation (LDA) or the generalized gradient approximation (GGA). More details can be found in the books mentioned in the introduction of the theory part. By minimizing the functional in Eq. 6 we get the Kohn-Sham equation

$$\left[-\frac{\hbar^2}{2m}\nabla^2 + \underbrace{V(\boldsymbol{r}) + e^2 \int \frac{n(\boldsymbol{r}')}{|\boldsymbol{r}-\boldsymbol{r}'|}d^3r' + \mu_{xc}[n(\boldsymbol{r})]}_{V_{\text{eff}}} \right]\Psi_i(\boldsymbol{r}) = \varepsilon_i\Psi_i(\boldsymbol{r}). \qquad (8)$$

With $\mu_{xc}[n(\boldsymbol{r})] = \frac{\partial E^{xc}[n(\boldsymbol{r})]}{\partial n(\boldsymbol{r})}$. Multiplying Eq. 8 by $\Psi_i^*(\boldsymbol{r})$, summing and integrating over the occupied states one can substitute the Kohn-Sham wavefunction in Eq. 6 to obtain the total energy

$$E = \sum_i \varepsilon_i - \frac{e^2}{2}\int\int \frac{n(\boldsymbol{r})n(\boldsymbol{r}')}{|\boldsymbol{r}-\boldsymbol{r}'|}d^3rd^3r' + \int n(\boldsymbol{r})\big[\varepsilon_{xc}[n(\boldsymbol{r})] - \mu_{xc}[n(\boldsymbol{r})]\big]d^3r. \qquad (9)$$

The set of Eqs. 89 is called Kohn-Sham equations. Eq. 8 can be solved with the DFT self-consistent cycle, see Fig. 7.

$$-\frac{1}{2}\nabla^2\Psi(\boldsymbol{r}) + V_{\text{eff}}(\boldsymbol{r})\Psi(\boldsymbol{r}) = \varepsilon\Psi(\boldsymbol{r})$$

$$V_{\text{eff}}(\boldsymbol{r}) \qquad\qquad n(\boldsymbol{r}) = \sum_i f_i |\Psi_i(\boldsymbol{r})|^2$$
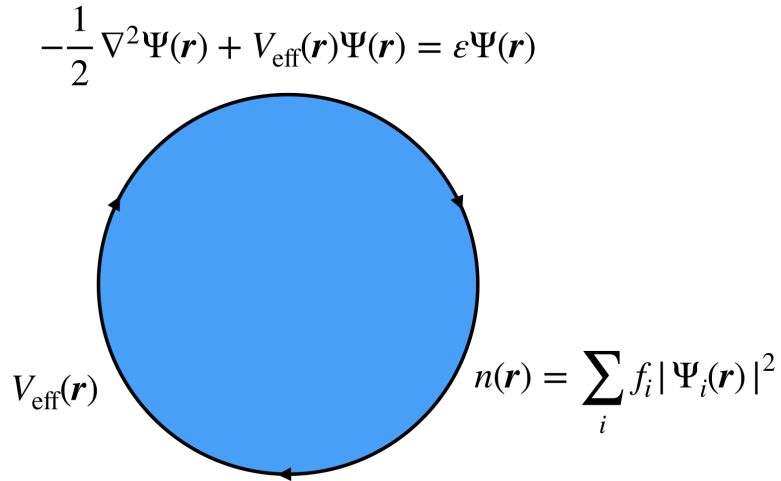
Figure 7: Self-consistent cycle LDA

Starting from a test density one obtains an effective potential V_{eff}. By mixing the initial density with the output density and solving the Kohn-Sham equation again, a new effective potential V_{eff} can be obtained. This cycle is repeated until the self-consistency is reached.

3.1.2 Bloch Functions: An Electron in a Periodic Potential

The Kohn-Sham equation, see Eq. 8, has the form of the Schrödinger equation for non-interacting electrons. By using atomic units $\hbar = 1$ and $m_e = 1$ the Kohn-Sham

equation simplifies to [50]

$$-\frac{1}{2}\nabla^2\Psi(\boldsymbol{r}) + V_{\text{eff}}(\boldsymbol{r})\Psi(\boldsymbol{r}) = \varepsilon\Psi(\boldsymbol{r}).\tag{10}$$

By defining $\Psi(\boldsymbol{r})$ as a normalizable function with periodic boundary conditions, Eq. 10 represents an eigenvalue problem $H\Psi = E\Psi$. $V_{\text{eff}}(\boldsymbol{r})$ is the crystal potential with translation symmetry $V_{\text{eff}}(\boldsymbol{r}) = V_{\text{eff}}(\boldsymbol{r} + \boldsymbol{R})$, where $\boldsymbol{R}$ is the crystal lattice vector. Then the Bloch theorem allows a partial diagonalization of the Hamiltonian H. The eigenfunctions of H can be written as the Bloch wave functions $\Psi_{n,\boldsymbol{k}}(\boldsymbol{r}) = e^{-i\boldsymbol{k}\cdot\boldsymbol{r}}u_{n,\boldsymbol{k}}(\boldsymbol{r})$ where $u_{n,\boldsymbol{k}}(\boldsymbol{r})$ is a $\boldsymbol{r}$-periodic function, n is a discrete band index and $\boldsymbol{k}$ a continuous vector from the first Brillouin zone. As already mentioned, Eq. 10 can be solved by the LDA self-consistent calculations. The LDA calculations within this thesis are performed with the software WIEN2k [53]. WIEN2k uses for the Bloch wave function a special basis in which the space is divided into non-overlapping spheres around atoms and the interstitial region, imaginable as a muffin-tin, see Fig. 8.
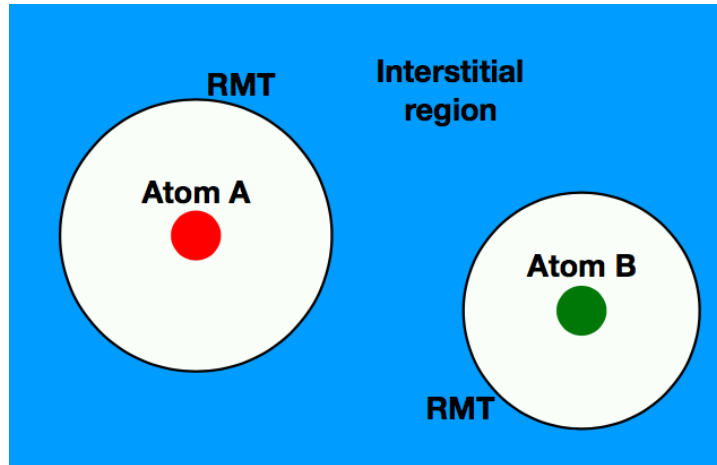

Figure 8: Muffin Tins

The spheres surrounding the atoms in the crystal with radius r_{RMT}. Within these the wave functions $\Psi_{n,\boldsymbol{k}}(\boldsymbol{r})$ are expanded in atomic-like orbitals, whereas in the interstitial region the wave functions are expressed as sum of plane waves. Inserting $\Psi_{n,\boldsymbol{k}}(\boldsymbol{r})$ into equation 10 results to following expression with periodic boundary conditions in the unit cell [50]

$$\frac{1}{2}(-i\nabla - \boldsymbol{k})^2 u_{n,\boldsymbol{k}}(\boldsymbol{r}) + V_{\text{eff}}(\boldsymbol{r})u_{n,\boldsymbol{k}}(\boldsymbol{r}) = \varepsilon_{n,\boldsymbol{k}}u_{n,\boldsymbol{k}}(\boldsymbol{r}).\tag{11}$$

The eigenvalues $\varepsilon_{n,\boldsymbol{k}}$ are continuous functions of $\boldsymbol{k}$. They form the "energy bands" in the bands model. A key characteristic of a band structure is the presence or absence of an energy gap separating occupied and unoccupied states, which characterizes an insulating or metallic behavior of the material, respectively. We classify different types of bands for the construction of Wannier functions in the following chapter 3.2. An isolated band has the property that it crosses with no other band at any k-point: $\varepsilon_{n-1,\boldsymbol{k}} < \varepsilon_{n,\boldsymbol{k}} < \varepsilon_{n+1,\boldsymbol{k}}$ for

each $\boldsymbol{k}$. Composite bands have the property of $\varepsilon_{n_{\min}-1,\boldsymbol{k}} < \varepsilon_{n_{\min},\boldsymbol{k}} \le \varepsilon_{n_{\max},\boldsymbol{k}} < \varepsilon_{n_{\max}+1,\boldsymbol{k}}$, whereas crossing bands are called entangled [50].

3.2 Wannier Functions

Wannier functions are widely used to link first-principle band structure calculations with model theories such as DMFT. The Wannier functions provide a natural extension of the concept of atomic orbitals into solids. They exhibit also fascinating aspects such like the connection between the spatial localization of Wannier functions and the topological properties of the corresponding Bloch states. In terms of Bloch states the dielectric polarization is expressed through the abstract concept of the Berry phase, where the formulation of Wannier functions uses a simple notion of the center of mass of the corresponding charge distribution. Many physical properties and phenomena involve spatially localized objects such as impurities, defects in crystal structure, screened electron-electron interaction or composite excitations [50].

A great advantage of Wannier functions for using them in model theories is their orthogonality on different lattice sites, compared to atomic functions. Wannier functions are constructed from the LDA calculated Bloch wave functions. For the construction of Wannier functions the classification of different types of bands introduced in the previous Ch. 3.1.2 becomes important.

The Wannier functions $w_n(\boldsymbol{r} - \boldsymbol{R})$ of isolated bands can be seen as the Fourier transformation of the Bloch functions $\Psi_{n,\boldsymbol{k}}(\boldsymbol{r})$ for the n-th band and are given by [50]

$$w_n(\boldsymbol{r} - \boldsymbol{R}) = \frac{V}{(2\pi)^3} \int_{BZ} d\boldsymbol{k} e^{-i\boldsymbol{k}\cdot\boldsymbol{R}} \Psi_{n,\boldsymbol{k}}(\boldsymbol{r}) \tag{12}$$

where V is the volume of the unit cell and the integrations runs over the first Brillouin zone. The Fourier transformation is not unique since the overall phase associated with the Bloch function is arbitrary. Therefore a particular choice of the phases, a so-called gauge, can be realized by a gauge transformation $\Psi_{n,\boldsymbol{k}} \to e^{i\phi(\boldsymbol{k})}\Psi_{n,\boldsymbol{k}}$. The inverse transformation results to the Bloch functions $\Psi_{n,\boldsymbol{k}}(\boldsymbol{r})$ and reads [50]

$$\Psi_{n,\boldsymbol{k}}(\boldsymbol{r}) = \sum_{\boldsymbol{R}} e^{i\boldsymbol{k}\cdot\boldsymbol{R}} w_n(\boldsymbol{r} - \boldsymbol{R}) \tag{13}$$

where the transformation properties of the Bloch functions under lattice translations $\Psi_{n,\boldsymbol{r}}(\boldsymbol{r}) = e^{-i\boldsymbol{k}\cdot\boldsymbol{r}} u_{n,\boldsymbol{k}}(\boldsymbol{r})$, see Ch. 3.1.2, ensure the orthogonality of Wannier functions centered in different unit cells.

The procedure of constructing Wannier functions for composite bands is similar [50]

$$\boldsymbol{w_n}(\boldsymbol{r} - \boldsymbol{R}) = \frac{V}{(2\pi)^3} \int_{BZ} d\boldsymbol{k} \boldsymbol{U}(\boldsymbol{k}) \boldsymbol{\Psi}_{n,\boldsymbol{k}}(\boldsymbol{r}), \tag{14}$$

where $\boldsymbol{w_n}(\boldsymbol{r} - \boldsymbol{R})$ and $\boldsymbol{\Psi}_{n,\boldsymbol{k}}(\boldsymbol{r})$ are vectors with the functions of the composite bands as the entries.

$$\boldsymbol{w} = \begin{pmatrix} w_{n_{min}} \\ \vdots \\ w_{n_{max}} \end{pmatrix}, \boldsymbol{\Psi_k} = \begin{pmatrix} \Psi_{n_{min},\boldsymbol{k}} \\ \vdots \\ \Psi_{n_{max},\boldsymbol{k}} \end{pmatrix} \tag{15}$$

A gauge transformation generalizes to a set of unitary transformations $U(k)$. If $U(k)$ can be chosen such that the product is an analytic and periodic function of k, one obtains exponentially localized Wannier functions. The inverse transformation results to so-called quasi-Bloch states and reads [50]

$$\tilde{\Psi}_k(r) = \sum_R e^{ik \cdot R} w(r - R) \qquad (16)$$

The quasi-Bloch functions have the transformation properties of the Bloch functions under lattice translation but are not eigenfunctions of the Hamiltonian anymore. The transformation of Bloch functions to Wannier functions, described so far, is a unitary transformation.

Generating Wannier functions for entangled bands is not a unitary transformation anymore, i.e. approximations are involved. We just mention here two methods which are used for transforming Bloch functions of entangled bands. The first method is proposed by Marzari and Vanderbilt [54], the maximally localized WF construction, where localized means how fast a function decays away from its center of mass. This method consists of finding a gauge in which the second moment of the density distribution is minimized. Another method is proposed by Ku et al. [55] where a projection of the Bloch states is used to construct Wannier functions. Both methods have in common that they start from a known set of Bloch eigenstates and search for a unitary transformation, see Eq. 14.
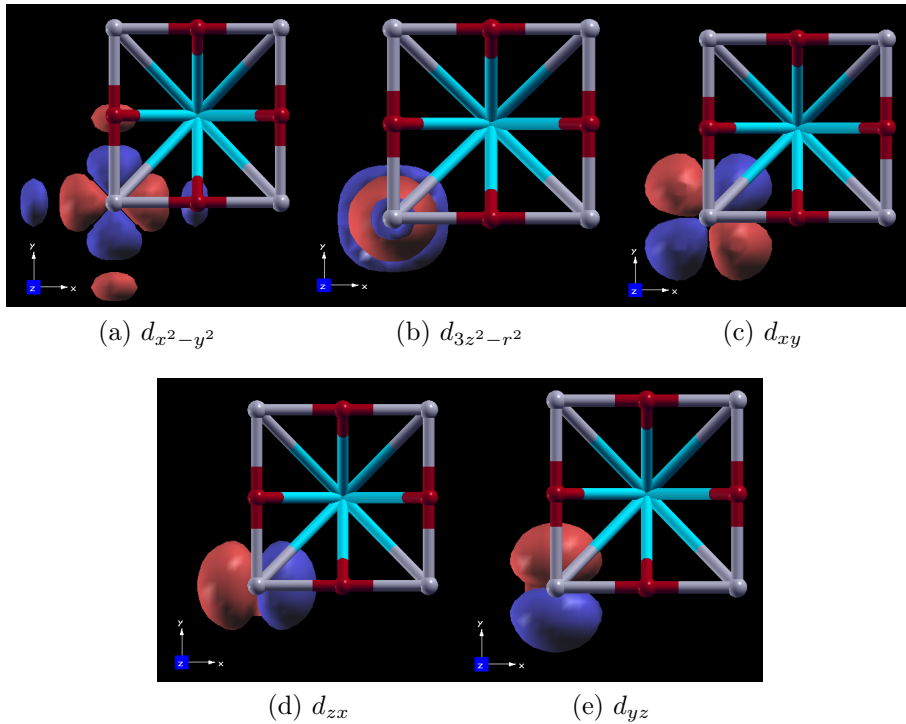

(a) $d_{x^2-y^2}$ (b) $d_{3z^2-r^2}$ (c) d_{xy}

(d) d_{zx} (e) d_{yz}

Figure 9: Ir d-orbital like Wannier Functions of the compound Sr_2IrO_4; XCrysDen [56]

Figure 9 shows the d-orbital like Wannier functions of Sr_2IrO_4. The Wannier functions are generated with the packages wien2wannier [48] and wannier90 [47] from a converged LDA cycle obtained by WIEN2k [53]). The displayed Wannier functions are maximally localized Wannier functions and plotted with XCrySDen [56]. In the following Ch. 3.3 we review the Hubbard model which is the basis of the DMFT calculations where the Wannier functions playing an important role for describing realistic systems.

3.3 Hubbard Model and dp Model

The single-band Hubbard model is a paradigm model for describing the electronic-correlation physics in TMO. The Hamiltonian of the Hubbard model is given by

$$\hat{H}_{\text{Hubbard}} = -t \sum_{\langle ij \rangle, \sigma} \left(\hat{c}^\dagger_{i,\sigma} \hat{c}_{j,\sigma} + \hat{c}^\dagger_{j,\sigma} \hat{c}_{i,\sigma} \right) + U \sum_i \hat{n}_{i,\uparrow} \hat{n}_{i,\downarrow}, \tag{17}$$

where the $\hat{c}^\dagger_{i,\sigma}$ and $\hat{c}_{i,\sigma}$ are creation and annihilation operators of electrons on the site (atom) i with spin σ, respectively. The first term describes the the hopping between adjacent atoms i and j, which favors delocalized states by an energy gain ($\sim t$). The second term is an interaction term and describes the Coulomb repulsion U between the electrons on the same atom i, with $n_{i,\sigma} = \hat{c}^\dagger_{i,\sigma} \hat{c}_{i,\sigma}$ being the density operator [3]. In general, the interaction term suppresses the on-site charge fluctuations. Therefore the Hubbard Hamiltonian describes two competing aspects of $3d$ electrons, *i.e.* itinerancy and the localization due to the presence of electronic interaction. The Hubbard model has the Mott-insulating solution, as we introduced in Ch. 2.1, which is believed to be realized in some TMO such as V_2O_3.

The dp model is a multi-orbital generalization of the Hubbard model and takes into account TM $3d$ and O $2p$ states explicitly. It includes the orbital degrees of freedom and the charge fluctuation between TM and oxygen $2p$ states. The dp model can describe the Mott insulator depending on the parameter values of the Coulomb interaction and the charge-transfer energy. In this thesis, we use the dp model constructed from the LDA calculation via the wannierization described above. The dp-Hamiltonian is given by

$$\hat{H}_{dp} = \sum_{i,\gamma,\sigma} \varepsilon_d(\gamma) \hat{d}^\dagger_{i,\gamma\sigma} \hat{d}_{i,\gamma\sigma} + \sum_{j,\lambda\sigma} \varepsilon_p(\lambda) \hat{p}^\dagger_{j,\lambda\sigma} \hat{p}_{j,\lambda\sigma} + \hat{T}_{pd} + \hat{T}_{dd} + \hat{T}_{pp} + \sum_i \hat{U}^{\text{int}}_i \tag{18}$$

where $\hat{d}^\dagger_{i,\gamma\sigma}$ ($\hat{p}^\dagger_{j,\lambda\sigma}$) and $\hat{d}_{i,\gamma\sigma}$ ($\hat{p}_{j,\lambda\sigma}$) are creation and annihilation operators of TM $3d$ (ligand $2p$) states, respectively. The first (second) term describes the on-site energy of the TM $3d$ (ligand $2p$) states on the site i (j). The index γ (λ) and σ denotes to the orbital and spin, respectively. The term $\hat{U}^{\text{int}}_i$ refers to the on-site Coulomb interaction between the TM $3d$ electrons on the same site i. The explicit form of $\hat{U}^{\text{int}}_i$ is given in [57, 3]. In the present study, the Coulomb interaction between O $2p$ electrons (and between O $2p$ and $3d$ electrons) is not considered explicitly. The operator $\hat{T}_{pd}$ refers to the hopping of electrons between d and p states [8]

$$\hat{T}_{pd} = \sum_{i,\gamma,j,\lambda,\sigma} t_{pd}(i,\gamma; j,\lambda) \left(\hat{d}^\dagger_{i,\gamma\sigma} \hat{p}_{j,\lambda\sigma} + \hat{p}^\dagger_{j,\lambda\sigma} \hat{d}_{i,\gamma\sigma} \right) \tag{19}$$

where $t_{pd}(i, \gamma; j, \lambda)$ is the hopping amplitude. The operators $\hat{T}_{dd}$ and $\hat{T}_{pp}$ denote the hopping between the TM $3d$ states and between the ligand $2p$ states, respectively [8].

$$\hat{T}_{dd} = \sum_{i,\gamma i',\gamma',\sigma} t_{dd}(i, \gamma; i', \gamma') \left(\hat{d}^{\dagger}_{i,\gamma\sigma} \hat{d}_{i',\gamma'\sigma} + \hat{d}^{\dagger}_{i',\gamma'\sigma} \hat{d}_{i,\gamma\sigma} \right) \tag{20}$$

$$\hat{T}_{pp} = \sum_{j\lambda j'\lambda'\sigma} t_{pp}(j, \lambda; j', \lambda') \left(\hat{p}^{\dagger}_{j,\lambda\sigma} \hat{p}_{j',\lambda'\sigma} + \hat{p}^{\dagger}_{j',\lambda'\sigma} \hat{p}_{j,\lambda\sigma} \right) \tag{21}$$

$t_{dd}(i, \gamma; i', \gamma')$ and $t_{pp}(j, \lambda; j', \lambda')$ are the hopping amplitudes. They describe the hopping between d (p) orbitals on different atoms i (j) and i' (j'), respectively.

3.4 Dynamical Mean Field Theory

Dynamical mean field theory (DMFT) is a many-body theory designed to describe electronic correlations in strongly correlated systems. In the DMFT approximation the energy dependence of the self-energy is taken into account explicitly but its momentum dependence is neglected, i.e. the self-energy is assumed to be a local quantity. In terms of the Feynman diagrams, all local skeleton diagrams are taken into account. Though this approximation is exact only in the limit of infinite dimensions, it is now widely accepted that it gives an accurate description of many aspects of 3-dimensional materials [4, 5, 44]. The core of DMFT is a self-consistent mapping of the fermionic Hubbard model onto the Anderson impurity model (AIM). The DMFT self-consistent condition requires that the impurity Green's function of the AIM and the local Green's function computed from the lattice Dyson equation are equal. Below we describe the AIM and the DMFT self-consistent calculation.

3.4.1 Anderson Impurity Model

The AIM is a single impurity model which is used to describe impurities embedded in a crystal host. The AIM takes into account a hybridization between the electronic states of the impurity and the states of the crystal host, represented by so-called bath states. The AIM is used for two applications within this thesis: (1) Within the DMFT self-consistent cycle where we map the dp model onto the AIM and (2) within the calculation of the spectral functions of the core-level X-ray spectroscopy, where the AIM is augmented by the TM $2p$ states. The AIM Hamiltonian is given by

$$\hat{H}_{\mathrm{AIM}} = \hat{H}_{\mathrm{imp}} + \hat{H}_{\mathrm{hyb}}, \tag{22}$$

where $\hat{H}_{\mathrm{imp}}$ is the on-site Hamiltonian of the impurity and $\hat{H}_{\mathrm{hyb}}$ describes the hybridization between the local states and the bath. The AIM is a single impurity model, thus we drop the cite indices i and j. The on-site Hamiltonian is given by [8]

$$\hat{H}_{\mathrm{imp}} = \sum_{\gamma} \varepsilon_d(\gamma) \hat{d}^{\dagger}_{\gamma} \hat{d}_{\gamma} + U_{dd} \sum_{\gamma > \gamma'} \hat{d}^{\dagger}_{\gamma} \hat{d}_{\gamma} \hat{d}^{\dagger}_{\gamma'} \hat{d}_{\gamma'} \tag{23}$$

$$- U_{dc} \sum_{\gamma,\eta} \hat{d}^{\dagger}_{\gamma} \hat{d}_{\gamma} (1 - \hat{c}^{\dagger}_{\eta} \hat{c}_{\eta}) + \hat{H}_{\mathrm{SO}} + \hat{H}_{\mathrm{Coulomb}}.$$

Here, $\hat{d}_\gamma^\dagger$ ($\hat{d}_\gamma$) and $\hat{c}_\eta^\dagger$ ($\hat{c}_\eta$) are the electron creation (annihilation) operators for TM $3d$ and TM $2p$ electrons with the flavor indices γ and η, respectively. By flavor we denote both the orbital and spin degrees of freedom. The natural bases, in which different parts of the Hamiltonian take a simple form, vary and will be stated explicitly in the following. For the numerical calculations are all terms of the Hamiltonian transformed into a common basis. The on-site Wannier state energies are denoted as $\varepsilon_d(\gamma)$. For the calculation of the spectral functions we consider the core hole created by the incident photon. Hence we augment the AIM Hamiltonian H_{AIM} by the interaction U_{dc} of the TM $2p$ and $3d$ orbitals. The monopole parts of the d–d (U_{dd}) and $2p$–$3d$ (U_{dc}) interactions are shown explicitly, while terms containing the multipole part of the Coulomb interaction and the SO interaction are described by the Hamiltonians $\hat{H}_{\mathrm{SO}}$ and $\hat{H}_{\mathrm{Coulomb}}$, respectively. We review in the following the crystal field splitting which lifts the degeneracy of the $3d$ states in the first term of Eq. 23, the spin-orbit interaction $\hat{H}_{\mathrm{SO}}$, the multipole part of the Coulomb interaction $\hat{H}_{\mathrm{Coulomb}}$ as well as hybridization part $\hat{H}_{\mathrm{hyb}}$ of the AIM Hamiltonian.

Crystal-Field Splitting: In a crystal, the five-fold degeneracy of the $3d$ states in spherical symmetry is removed by the static electric field produced by the ligands and the rest of the crystal, the so-called crystal-field splitting. In octahedral symmetry (O_h), the $3d$ energy levels split into doubly-degenerate e_g states and triply-degenerate t_{2g} states. The energy splitting between e_g and t_{2g} is represented by Δ_{CF} or often $10Dq$, as introduced in Ch. 2.2.2. Then, for the average energy E_d ($\equiv$ the center of gravity of $3d$ levels), the energies of the e_g and t_{2g} states are given by [3, 8]

$$\varepsilon_d(e_g) = \varepsilon_d + \frac{3}{5}\Delta_{\mathrm{CF}} = \varepsilon_d + 6Dq \tag{24}$$

$$\varepsilon_d(t_{2g}) = \varepsilon_d - \frac{2}{5}\Delta_{\mathrm{CF}} = \varepsilon_d - 4Dq \tag{25}$$

The explicit form of the two irreducible representations are e_g: $d_{3z^2-r^2}$, $d_{x^2-y^2}$ and t_{2g}: d_{xy}, d_{yz}, d_{zx}, where the orthogonal axes (x, y, z) point from the TM ion to the neighboring ligands (in a MO$_6$ cluster). In terms of the spherical-harmonics basis Y_γ^l they take the following form

$$d_{3z^2-r^2} = Y_0^2, \qquad d_{x^2-y^2} = \frac{1}{\sqrt{2}}(Y_2^2 + Y_{-2}^2)$$

$$d_{xy} = \frac{-i}{\sqrt{2}}(Y_2^2 - Y_{-2}^2), \qquad d_{yz} = \frac{i}{\sqrt{2}}(Y_1^2 - Y_{-1}^2), \qquad d_{zx} = \frac{-1}{\sqrt{2}}(Y_1^2 - Y_{-1}^2)$$

For example, the Wannier functions for Ir $5d$ states in Sr$_2$IrO$_4$ are shown in Fig. 9. In the present LDA+DMFT approach the crystal field splitting is not an adjustable parameter, as in the cluster-model analysis, but determined by the *ab-initio* band structure.

Spin-Orbit Interaction: The spin-orbit (SO) coupling is a relativistic effect which occurs predominately in the core states (~ 10 eV), such as the TM $2p$ states. In valence

states the SO interaction is weak ($\sim$ a few 100 meV). The spin-orbit interaction of electrons is given by [8]

$$\hat{H}_{\text{SO}} = \sum_l \underbrace{\zeta_l \sum_{\gamma,\gamma'} \langle \gamma | \boldsymbol{l} \cdot \boldsymbol{s} | \gamma' \rangle \, \hat{a}^\dagger_\gamma \hat{a}_{\gamma'}}_{\hat{h}_{\text{SO}}(l)} \tag{26}$$

where $\boldsymbol{l}$ and $\boldsymbol{s}$ are the angular momentum and the spin operators, respectively. $\hat{a}^\dagger_{\gamma\sigma}$ ($\hat{a}_{\gamma\sigma}$) are the creation (annihilation) operator for electrons. The indices γ and γ' denote to the magnetic quantum number of the l-th subshell and to the spin in the range of $-s, s+1, \ldots, s$. The spin-orbit coupling constant ζ_l is represented by

$$\zeta_l = \frac{1}{2}\alpha^2 \int_0^\infty R_l^2(r) \frac{1}{r}\frac{dV}{dr} r^2 dr \tag{27}$$

were the electronic potential $V(r)$ acts on the electrons in the l-th subshell with the radial part $R_l(r)$ of the $|\gamma'\sigma'\rangle$ state. The constant α is the relativistic fine-structure constant. Using the Wigner-Eckart theorem, $\hat{h}_{\text{SO}}(l)$ is given in diagonal form by

$$\hat{h}_{\text{SO}}(l) = \sum_{j,m} \varepsilon(j)\hat{a}^\dagger_{jm}\hat{a}_{jm}, \tag{28}$$

where $j = l + s$ is the total angular momentum, in the range from $|l - s| \le j \le l + s$ in steps of one, and m the z-component of the total angular momentum in the range of $-j, j+1, \ldots, +j$. The energy is given by

$$\varepsilon(j) = \begin{cases} \zeta_l \cdot l/2 & (j = l + 1/2) \\ -\zeta_l \cdot (l+1)/2 & (j = l - 1/2) \end{cases}. \tag{29}$$

Multipole Part of the Coulomb Interaction: The multipole parts are the difference between the average Coulomb interaction and the actual one, which depends on the shape of the respective orbitals. The multipole parts are derived from the Taylor expansion of the Coulomb interaction. To describe the atomic multiplet structures in XAS spectra quantitatively the multipole parts of the Coulomb interaction have to be explicitly considered. In our approach we apply the Coulomb interaction for partially filled 3d shells and the Coulomb interaction between TM 3d and TM 2d shells. Hence the Hamiltonian for the multipole parts of the Coulomb interaction is given as [8]

$$\hat{H}_{\text{Coulomb}} = \hat{H}_{3d-3d} + \hat{H}_{2p-3d}, \tag{30}$$

where $\hat{H}_{3\text{d}-3\text{d}}$ describes the Coulomb interaction of the 3d electrons and $\hat{H}_{2p-3d}$ the Coulomb interaction between the TM 2p and TM 3d electrons. We use here spherical harmonics, therefore the index γ represents the magnetic and the spin quantum number of the corresponding 3d-shell $l = 2$. The Coulomb multiplet interaction of 3d–3d orbitals is given as

$$\hat{H}_{3d-3d} = \sum_{\gamma<\gamma',\gamma''<\gamma'''} \left[\langle \gamma\gamma' | \frac{1}{r_{12}} | \gamma''\gamma''' \rangle - \langle \gamma\gamma' | \frac{1}{r_{12}} | \gamma'''\gamma'' \rangle \right] \hat{d}^\dagger_\gamma \hat{d}^\dagger_{\gamma'} \hat{d}_{\gamma'''} \hat{d}_{\gamma''}. \tag{31}$$

The distance between the electrons is given as $r_{12} = |\boldsymbol{r}_2 - \boldsymbol{r}_1|$. The first and second term in the square brackets are the direct and the exchange integrals of the Coulomb interaction, respectively. By the use of spherical coordinates the Coulomb interaction $\frac{1}{r_{12}}$ is expressed as [50]

$$\frac{1}{r_{12}} = \sum_k \frac{r_<^k}{r_>^{k+1}} \frac{4\pi}{2k+1} \sum_{q=-k}^{k} Y_q^k(\theta_2, \phi_2) \bar{Y}_q^k(\theta_1, \phi_1) \tag{32}$$

where $r_>$ and $r_<$ means the larger and smaller ones of r_1 and r_2. Y_q^k are the spherical harmonics. The direct integral results to [8]

$$\langle \gamma\gamma' | \frac{1}{r_{12}} | \gamma''\gamma''' \rangle = \sum_k F^k(3d, 3d) f^k(\gamma\gamma', \gamma''\gamma''') \tag{33}$$

where $F^k(3d, 3d)$ is the Slater integral and is given in terms of the radial part of the $3d$ orbitals as

$$F^k(3d, 3d) = \int_0^\infty \int_0^\infty R_{3d}^2(r_1) R_{3d}^2(r_2) \frac{r_<^k}{r_>^{k+1}} r_1^2 r_2^2 dr_1 dr_2 \tag{34}$$

and $f^k(\gamma\gamma', \gamma''\gamma''')$ are the angular integrals

$$f^k(\gamma\gamma', \gamma''\gamma''') = \sum_q (-1)^q \langle \gamma | C_{-q}^k | \gamma'' \rangle \langle \gamma' | C_q^k | \gamma''' \rangle \tag{35}$$

with the the spherical function C_q^k operator, which is defined from the spherical harmonics $Y_q^k(\theta, \phi)$ as

$$C_q^k(\theta, \phi) = \sqrt{\frac{4\pi}{2k+1}} Y_q^k(\theta, \phi) \tag{36}$$

The natural basis to evaluate Eq. 35 is the spherical harmonics basis. With the Wigner-Eckart theorem we derive that $k = 0, 2, 4$ is satisfying Eq. 35. $k = 0$ corresponds to the monopole part which is already taken into account in the Coulomb term U_{dd} of Eq. 22. The terms $k = 2, 4$ contribute to the multipole part of the $3d$–$3d$ interaction where the Hamiltonian is given as [8]

$$\hat{H}_{3d-3d} = \sum_{k=2,4} F^k(3d, 3d) \sum_{\gamma<\gamma', \gamma''<\gamma'''} \left[f^k(\gamma\gamma', \gamma''\gamma''') - f^k(\gamma\gamma', \gamma'''\gamma'') \right] \hat{d}_\gamma^\dagger \hat{d}_{\gamma'}^\dagger \hat{d}_{\gamma'''} \hat{d}_{\gamma''}. \tag{37}$$

The multipole parts of the Coulomb interaction between $2p$ shells and $3d$ shells are similar to the multipole parts given in $\hat{H}_{3d-3d}$, but to derive these takes more effort. We present the Hamiltonian $\hat{H}_{2d-3d}$ as [8]

$$\begin{aligned} \hat{H}_{2d-3d} &= \sum_{\eta,\gamma,\eta',\gamma'} \left[\langle \eta\gamma | \frac{1}{r_{12}} | \eta'\gamma' \rangle - \langle \eta\gamma | \frac{1}{r_{12}} | \gamma'\eta' \rangle \right] \hat{c}_\eta^\dagger \hat{c}_{\eta'} \hat{d}_\gamma^\dagger \hat{d}_{\gamma'} \\ &= F^2(2p, 3d) \sum_{\eta,\gamma,\eta',\gamma'} f^2(\eta\gamma, \eta'\gamma') \hat{c}_\eta^\dagger \hat{c}_{\eta'} \hat{d}_\gamma^\dagger \hat{d}_{\gamma'} \\ &\quad - \sum_{k=1,3} G^k(2p, 3d) \sum_{\eta,\gamma,\eta',\gamma'} f^k(\eta\gamma, \gamma'\eta') \hat{c}_\eta^\dagger \hat{c}_{\eta'} \hat{d}_\gamma^\dagger \hat{d}_{\gamma'}, \end{aligned} \tag{38}$$

where index γ represents the magnetic and the spin quantum number of the corresponding 2p-shell $l = 1$. The monopole term with $k = 0$ is already taken into account in the U_{dc} of equation 23 and therefore omitted. The Slater integrals or interaction parameters $F^k(2p, d)$ and $G^k(2p, d)$ have the following form [8]

$$F^k(2p, 3d) = \int_0^\infty \int_0^\infty R_{2p}^2(r_1) R_{3d}^2(r_2) \frac{r_<^k}{r_>^{k+1}} r_1^2 r_2^2 dr_1 dr_2 \qquad (39)$$

$$G^k(2p, 3d) = \int_0^\infty \int_0^\infty R_{2p}(r_1) R_{3d}(r_1) R_{2p}^2(r_2) R_{3d}(r_2) \frac{r_<^k}{r_>^{k+1}} r_1^2 r_2^2 dr_1 dr_2, \qquad (40)$$

where the anisotropic part of the 2p–3d interaction parameters $F^k(2p, 3d)$, $G^k(2p, 3d)$ can be calculated with an atomic Hartree-Fock code.

We give here few comments to the Slater integrals which are taken as parameters in our calculations. The monopole part of the Coulomb interaction U_{dd} and U_{dc} is substantially screened from its bare value. The screened value of U_{dd} can be estimated using the constrained random-phase approximation (cRPA), LDA (cLDA) [50], or by fitting the valence photoemission spectra. However the screened value of U_{dc} is hard to be determined in an *ab*-initio way. So, in the present study, we fix $U_{dc} = 0.80 \times U_{dd}$ by an empirical estimate based on comparison to many spectra. The choice of the parameters for the multipole part of the Coulomb interaction is different. In general, the screening is less important for the higher-order Slater integrals. For the interaction between 3d electrons, the cRPA or cLDA gives a reasonable estimation for Hund's J that relates to the Slater integrals F^2 and F^4 as $J = (F^2 + F^4)/14$. By assuming $F^4 = 0.625 \times F^2$ which is valid for atomic radial functions we can obtain the Slater-integral values. Though the Slater-intergrals for the core-valence interactions could be estimated using the radial integral using the Wannier functions, we take the values obtained from the atomic Hartree-Fock calculation, for the sake of simplicity.

Hybridization: $\hat{H}_{\mathrm{hyb}}$ includes the hybridization of the on-site TM 3d (impurity) states with the fermionic bath of the crystal, described by auxiliary states, and is given as

$$\hat{H}_{\mathrm{hyb}} = \underbrace{\sum_{\alpha, \gamma} \varepsilon_{\alpha\gamma} \hat{b}_{\alpha\gamma}^\dagger \hat{b}_{\alpha\gamma}}_{\hat{H}_{\mathrm{host}}} + \underbrace{\sum_{\alpha, \gamma} v_{\alpha\gamma} (\hat{d}_\gamma^\dagger \hat{b}_{\alpha\gamma} + \hat{b}_{\alpha\gamma}^\dagger \hat{d}_\gamma)}_{\hat{H}_{\mathrm{loc-host}}}. \qquad (41)$$

The first term $\hat{H}_{\mathrm{host}}$ represents the energies of the auxiliary states $|\hat{b}_{\alpha\gamma}\rangle$. The index α represents the auxiliary states and the index γ represents the irreducible representation of the impurity orbitals in terms of the point group of the impurity site including the spin index. The second term $\hat{H}_{\mathrm{loc-host}}$ describes the hopping between the impurity orbital and the auxiliary states with the amplitude $v_{\alpha\gamma}$. Here $\hat{b}_{\alpha\gamma}^\dagger$ ($\hat{b}_{\alpha\gamma}$) is the creation (annihilation) operator for the auxiliary state with energy $\varepsilon_{\alpha\gamma}$. The hybridization is assumed to be orbital and spin diagonal, which is a good approximation in the studied materials and

can be exact for a high site symmetry. The hybridization function which we obtain from the DMFT self-consistent cycle is given by [15]

$$\Delta_{\gamma\gamma}(\varepsilon) = \sum_{\alpha} \frac{v_{\alpha\gamma}^2}{\varepsilon - \varepsilon_{\alpha\gamma}}, \tag{42}$$

where $\Delta_{\gamma\gamma}(\varepsilon)$ describes the hybridization of an impurity orbital with the rest of the crystal.

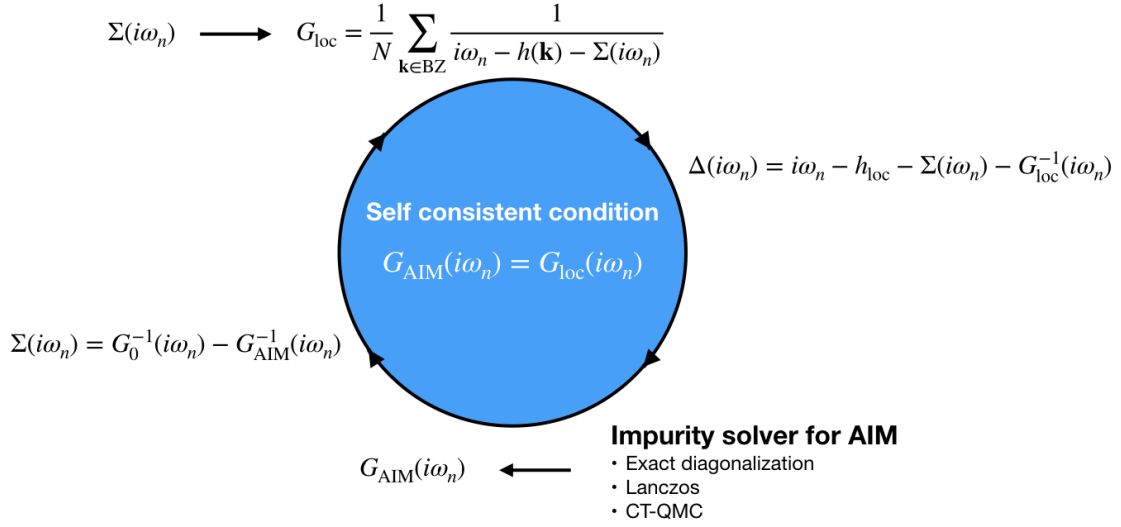### 3.4.2 DMFT Self-Consistent Cycle and Hybridization Function

$$\Sigma(i\omega_n) \longrightarrow G_{\text{loc}} = \frac{1}{N} \sum_{\mathbf{k} \in \text{BZ}} \frac{1}{i\omega_n - h(\mathbf{k}) - \Sigma(i\omega_n)}$$

$$\Delta(i\omega_n) = i\omega_n - h_{\text{loc}} - \Sigma(i\omega_n) - G_{\text{loc}}^{-1}(i\omega_n)$$

Self consistent condition

$$G_{\text{AIM}}(i\omega_n) = G_{\text{loc}}(i\omega_n)$$

$$\Sigma(i\omega_n) = G_0^{-1}(i\omega_n) - G_{\text{AIM}}^{-1}(i\omega_n)$$

$$G_{\text{AIM}}(i\omega_n) \longleftarrow$$

Impurity solver for AIM
- Exact diagonalization
- Lanczos
- CT-QMC

Figure 10: DMFT cycle, adapted from [58] with the permission of author

We describe here the self-consistent calculation in the LDA+DMFT scheme. Fig. 10 is a sketch of the DMFT self-consistent cycle. We start with an initial guess of the local self-energy $\Sigma(i\omega_n)$ of TM $3d$ states. Here, $\omega_n = (2n + 1)\pi/\beta$ ($n \in \mathbf{Z}$) are the Matsubara frequencies. The self-energy describes the electron dynamics due to the Coulomb interaction on the TM sites. Then the self-energy is applied to the TM $3d$ bands in the dp model and the local Green's function $G_{\text{loc}}(i\omega_n)$ is computed by taking the average of the lattice Green's function over the Brillouin zone and use the part of the on-site d orbitals

$$G_{\text{loc}}^{\gamma\gamma'}(i\omega_n) = \frac{1}{N} \sum_{\mathbf{k} \in \text{BZ}} [i\omega_n - h(\mathbf{k}) - \Sigma(i\omega_n)]_{\gamma\gamma'}^{-1}. \tag{43}$$

Here $h(\mathbf{k})$ is the lattice Fourier transformation of the one-electron Hamiltonian h. The one-electron Hamiltonian h is the hopping matrix of the dp Hamiltonian, see Eq. 18. $\Sigma(i\omega_n)$ acts only on the d-subspace. The hybridization function $\Delta(i\omega_n)$ is obtained by

$$\Delta(i\omega_n) = i\omega_n - h_{\text{loc}} - \Sigma(i\omega_n) - G_{\text{loc}}^{-1}(i\omega_n), \tag{44}$$

with $h_{\mathrm{loc}}^{\gamma\gamma'} = \frac{1}{N} \sum_{\boldsymbol{k} \in \mathrm{BZ}} h_{\gamma\gamma'}(\boldsymbol{k})$. The orbital and spin indices are dropped off, for simplicity. The AIM is given by h_{loc} and the hybridization function. In practice, we employ the continuous-time quantum Monte Carlo (CT-QMC) method to solve the AIM. The CT-QMC is a well-established impurity solver for multi-orbital systems. We use the in-house CT-QMC package, which implements recent improved estimator techniques [59, 60, 61]. The self-energy is recomputed from the Green's function $G_{\mathrm{AIM}}(i\omega_n)$ of the AIM with the hybridization function and the non-interacting Green's function G_0. This cycle is repeated till the DMFT self-consistent condition $G_{\mathrm{AIM}}(i\omega_n) = G_{\mathrm{loc}}(i\omega_n)$ is satisfied with a converged self-energy $\Sigma(i\omega_n)$. After the convergence is obtained, we perform the analytic continuation to obtain $\Sigma(\varepsilon)$ along the real-frequency domain. We employ the maximum entropy method directly to the self-energy $\Sigma(\varepsilon)$ and finally obtain the continuous hybridization function $\Delta(\varepsilon)$ to compute core-level spectra. In the studied compounds, the hybridization function is as an approximation diagonal, as already mentioned in Ch. 3.4.1. The hybridization strength in Eq. 42 is computed by the imaginary part of the hybridization function.

3.5 Core-Level Spectroscopy Calculation using DMFT-based Anderson Impurity Model

We describe below the computational details of a core-level spectroscopy calculation. In the present approach based on LDA+DMFT, the core-level spectra are calculated using the Anderson impurity model (AIM) with the DMFT hybridization intensity. The AIM is augmented by the core states which are excited by the incident photons. The localized core states strongly interact with the $3d$ states on the excited transition metal. Thus, for a quantitative analysis of core-level spectra, the Coulomb multiplet interaction between the core and $3d$ states, see Eq. 38, should be taken into account properly. Here one cannot employ the continuous-time Quantum Monte Carlo method, that is used in the self-consistent calculation of LDA+DMFT, see Ch. 3.4.2, since the analytic continuation of the imaginary-frequency $i\omega$ to the real-frequency domain smears out these multiplet features, making a comparison to high-resolution experimental data impossible. To overcome the difficulty, A. Hariki and T. Uozumi proposed a different route and developed an impurity solver based on the configuration-interaction (CI) scheme [62]. This impurity solver works directly in the real-frequency domain and takes into account the full Coulomb multiplet interaction as well as the spin-orbit interaction. The CI scheme provides a systematic way to construct an appropriate set of the many-body Slater determinants which is necessary to describe the ground state and the excited states involved by the core-level excitation accurately [42].
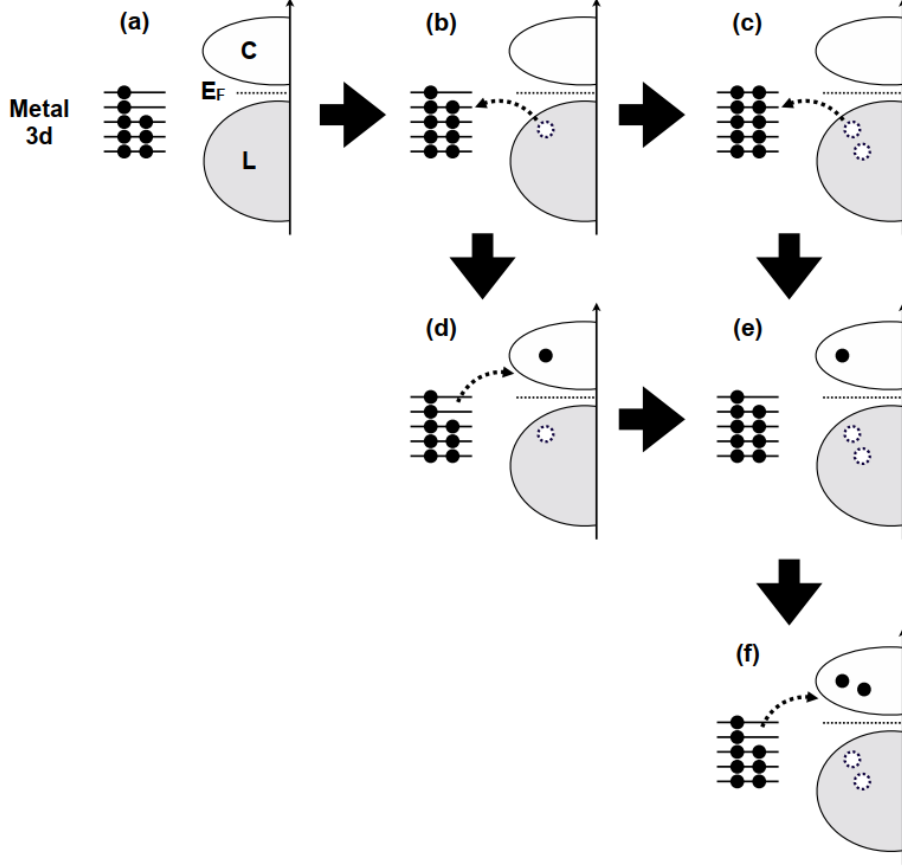
Figure 11: Schematic representation of basis construction in the CI scheme for a $3d$ system with 8 electrons in the $3d$ shell in the nominal valence. Starting from (a) $|d^8\rangle$ configuration, electronic configurations (b) $|d^9\underline{L}^1\rangle$, (c) $|d^{10}\underline{L}^2\rangle$, (d) $|d^8\underline{L}^1c'^1\rangle$, (e) $|d^9\underline{L}^2c'^1\rangle$ and (f) $|d^8\underline{L}^2c'^2\rangle$ are constructed through the hybridization interaction. Figure adapted from [8] with the permission of the author

In the present CI scheme, the many-body wave function is represented by a linear combination of the electronic configurations of the AIM. Following the early study by Gunnarsson and Schönhammer [42], the configuration is denoted symbolically as $|d^n\underline{L}^m c'^l\rangle$, that collectively denotes the many-body Slater determinants with "n"-electrons in the $3d$ shell, "m"-holes in valence states, and "l"-electrons in the conduction states. We note here that, in this thesis, the valence and conduction state refer to the states below and above the Fermi-level E_F in the density of states, respectively. Thus the valence state includes not only ligand states but also (occupied) TM $3d$ states. These configurations are successively constructed by the electron charge-transfer from the bath state to the TM state or vice versa, starting with the configuration with the filled ligand state, see Fig. 11. The basis configuration is collectively denoted as $|d^n\rangle$ where $\binom{10}{n}$ electronic configuration are included. Further configurations involve the filling of the TM $3d$ shell with

electrons of the ligand bath, in our present CI scheme up to two additional electrons, see Fig. 11(b,c). This is in the most scenarios sufficient due to the increasing energy costs of transferring the ligand electrons to the TM $3d$ states and to limit the computational costs. The number of basis states in each configuration increases exponentially with the number of holes in the valence bath. The states in Fig. 11(d,e,f) contain the charge transfer from the TM $3d$ shell into the conduction bath. A ground state of a system is written as follows

$$|g\rangle = a_0 \, |d^n\rangle + a_1 \, |d^{n+1}\underline{L}\rangle + a_2 \, |d^{n+2}\underline{L}^2\rangle + a_3 \, |d^n\underline{L}c'\rangle + ... \tag{45}$$

For $T > 0$ a set of initial states are calculated by the low-energy states, weighted with the Boltzmann factor $e^{-E_n/k_B T}$

$$|n\rangle = a_0' \, |d^n\rangle + a_1' \, |d^{n+1}\underline{L}\rangle + a_2' \, |d^{n+2}\underline{L}^2\rangle + a_3' \, |d^n\underline{L}c'\rangle + ... \tag{46}$$

The initial state is calculated by the AIM Hamiltonian H_{AIM} using the Lanczos algorithm. The one-particle basis of $3d$ states on the TM ion are the Wannier functions, introduced in Ch. 3.2, consistently employed with the LDA+DMFT calculation. The final state is represented similarly, but for e.g. XPS a hole in the core states, denoted as $|\underline{c}\rangle$, is considered

$$|f_{\mathrm{XPS}}\rangle = c_0 \, |\underline{c}d^n\rangle + c_1 \, |\underline{c}d^{n+1}\underline{L}\rangle + c_2 \, |\underline{c}d^{n+2}\underline{L}^2\rangle + c_3 \, |\underline{c}d^n\underline{L}c'\rangle + ... \tag{47}$$

3.5.1 X-Ray Photoemission Spectroscopy

$2p$ XPS is described by a transition from the ground state $|g\rangle$ to a final state $|f\rangle$. For simplicity we assume that the temperature is $T = 0$ K.

$$\underbrace{|g\rangle}_{\text{ground state}} \quad \rightarrow \quad \underbrace{\hat{T}_{\mathrm{D}}}_{\text{transition}} \quad \rightarrow \quad \underbrace{|f\rangle}_{\text{final state}}$$

The transition operator $\hat{T}_{\mathrm{D}}$ describes the response of the system to the incident photon that creates a $2p$ core hole and a photoelectron. $\hat{T}_{\mathrm{D}} \sim \boldsymbol{\varepsilon} \cdot \hat{\boldsymbol{r}}$ is the dipole operator which is proportional to the product of the position operator $\hat{\boldsymbol{r}}$ and the polarization vector $\boldsymbol{\varepsilon}$ in the long range wave limit. The spectral function $F_{\mathrm{XPS}}(\omega_k)$ of an $2p$ XPS process, already introduced in the Ch. 2.2.2, is given by Fermi's golden rule

$$F_{\mathrm{XPS}}(\omega_k) = \sum_f |\langle f|\hat{T}_{\mathrm{D}}|g\rangle|^2 \delta(E_g + \hbar\omega_k - E_f), \tag{48}$$

where ω_k denotes to the emitted electron. The ground $|g\rangle$ and final states $|f\rangle$ are computed within the CI-scheme in the present approach. The Dirac delta function $\delta(E_g + \hbar\omega_k - E_f)$ represents the energy conservation. The energy of the ground E_g and final state E_f are calculated with the AIM Hamiltonian $\hat{H}_{\mathrm{AIM}}$, see Eq. (22). Then at

finite temperature $T > 0$ K, one should sum up contributions from different initial states $|n\rangle$ with the Boltzmann factor $e^{-E_n/k_B T}$,

$$F_{\text{XPS}}(\omega_k) = \sum_n F_{\text{XPS}}^{(n)}(\omega_k) \times \frac{e^{-E_n/k_B T}}{Z} \tag{49}$$

where

$$F_{\text{XPS}}^{(n)}(\omega_k) = \sum_f \left| \langle f | \hat{T}_{\text{D}} | n \rangle \right|^2 \delta(E_n + \hbar\omega_k - E_f). \tag{50}$$

Here Z is the distribution function of the system.

3.5.2 X-Ray Absorption Spectroscopy

The computational details of $2p$ XAS differs to them of $2p$ XPS due to the absorption of the incident photon. The transition reads formally similar

$$\underbrace{|n\rangle}_{\text{initial state}} \rightarrow \underbrace{\hat{T}_{\text{D}}}_{\text{absorption}} \rightarrow \underbrace{|f\rangle}_{\text{final state}} .$$

In XAS the transition operator $\hat{T} \sim \boldsymbol{\varepsilon} \cdot \hat{\boldsymbol{r}}$ is the dipole operator within the E1 dipole approximation. The initial state $|n\rangle$ is computed within the CI scheme and has the form

$$|n\rangle = a_0 |d^n\rangle + a_1 |d^{n+1}\underline{L}\rangle + a_2 |d^{n+2}\underline{L}^2\rangle + a_3 |d^n\underline{L}c'\rangle + \dots. \tag{51}$$

The final state $|n\rangle$ of XAS includes the core excited electron

$$|f\rangle = a_0' |\underline{c}d^{n+1}\rangle + a_1' |\underline{c}d^{n+2}\underline{L}\rangle + a_2' |\underline{c}d^{n+3}\underline{L}^2\rangle + a_3' |\underline{c}d^{n+1}\underline{L}c'\rangle + \dots. \tag{52}$$

We consider here that if the $d^{n=10}$ state is fully occupied, the state $d^{(n=10)+1}$ does not exist. The spectral function of $2p$ XAS F_{XAS}, reviewed in Ch. 2.2.2, reads

$$F_{\text{XAS}}^{(n)}(\omega_k) = \sum_f \left| \langle f | \hat{T}_{\text{D}} | n \rangle \right|^2 \delta(E_n + \hbar\omega_k - E_f), \tag{53}$$

where ω_k denotes to the incident photon energy and the Dirac delta function describes the energy conservation. For finite temperatures we sum over the contributions of different initial states, weighted by the Boltzmann factor and the partition function

$$F_{\text{XAS}}(\omega_k) = \sum_n F_{\text{XAS}}^{(n)}(\omega_k) \times \frac{e^{-E_n/k_B T}}{Z}. \tag{54}$$

3.5.3 Resonant Inelastic X-ray Scattering

We review here the the computational details of L-edge ($2p \rightarrow 3d \rightarrow 2p$) RIXS with the scattering geometry. Within the RIXS process we consider an intermediate state due to the absorption and the subsequent emission of a photon.

$$\underbrace{|n\rangle}_{\text{initial state}} \rightarrow \underbrace{\hat{T}_{\text{I}}}_{\text{absorption}} \rightarrow \underbrace{|m\rangle}_{\text{intermediate state}} \rightarrow \underbrace{\hat{T}_{\text{E}}}_{\text{emission}} \rightarrow \underbrace{|f\rangle}_{\text{final state}}$$

The initial state $|n\rangle$ is transfered by the transition operator $\hat{T}_\mathrm{I}$ into an intermediate state similar to the final state of XAS. The subsequent emission of a photon is described by the transition from the intermediate state $|n\rangle$ to the final state $|f\rangle$ by the transition operator $\hat{T}_\mathrm{E}$. $\hat{T}_\mathrm{I}$ and $\hat{T}_\mathrm{E}$ are dipole operators. The initial state of RIXS has the form

$$|n\rangle = a_0 \, |d^n\rangle + a_1 \, |d^{n+1}\underline{L}\rangle + a_2 \, |d^{n+2}\underline{L}^2\rangle + a_3 \, |d^n\underline{L}c'\rangle + a_4 \, |d^{n+1}\underline{L}^2c'\rangle + \ldots. \tag{55}$$

The intermediate state coincides with the final state of XAS

$$|m\rangle = a_0' \, |\underline{c}d^{n+1}\rangle + a_1' \, |\underline{c}d^{n+2}\underline{L}\rangle + a_2' \, |\underline{c}d^{n+3}\underline{L}^2\rangle + a_3' \, |\underline{c}d^{n+1}\underline{L}c'\rangle + a_4' \, |\underline{c}d^{n+2}\underline{L}^2c'\rangle + \ldots. \tag{56}$$

In the final state the core-hole is occupied with an electron due to the relaxation process and thus the final state reads

$$|f\rangle = a_0'' \, |d^n\rangle + a_1'' \, |d^{n+1}\underline{L}\rangle + a_2'' \, |d^{n+2}\underline{L}^2\rangle + a_3'' \, |d^n\underline{L}c'\rangle + a_4'' \, |d^{n+1}\underline{L}^2c'\rangle + \ldots. \tag{57}$$

To simulate the experimental setup we review the scattering plane of RIXS, see Fig. 12.
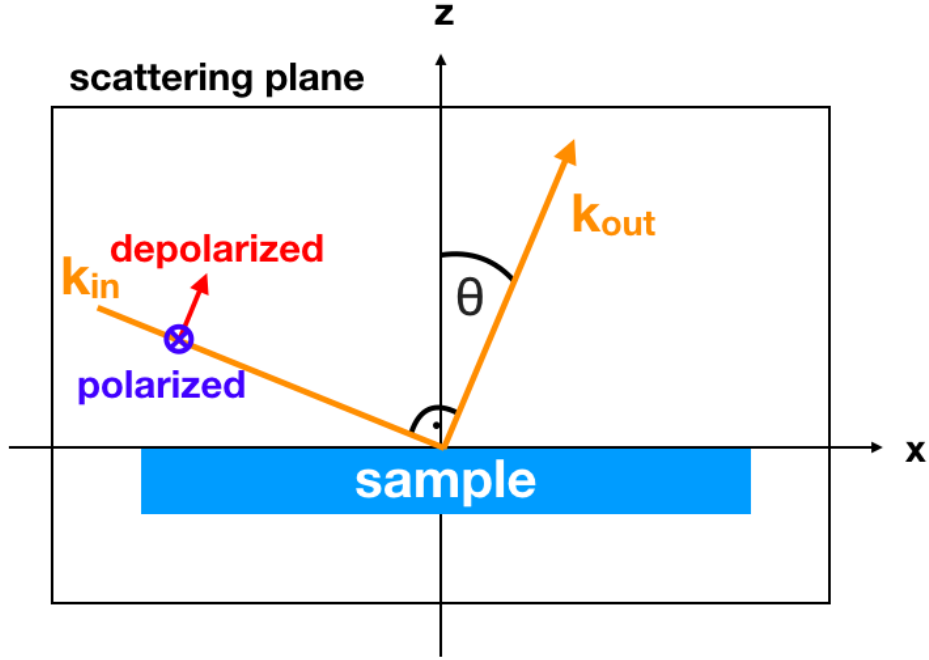
Figure 12: RIXS scattering process with polarization. The polarization of the incident photon lies either in or perpendicular to the scattering plane

The scattering plane is spanned by the orthogonal wave vectors of the incident $\boldsymbol{k}_\mathrm{in}$ and emitted $\boldsymbol{k}_\mathrm{out}$ photon. θ is defined as the angle between the z-direction and the outgoing wave vector $\boldsymbol{k}_\mathrm{out}$. In spectroscopic nomenclature there are two cases of polarization for the incident photon $\boldsymbol{k}_\mathrm{in}$,

polarized: the polarization vector is perpendicular to the scattering plane

depolarized: the polarization vector lies on the scattering plane

The spectral function of RIXS $F_{\text{RIXS}}(\omega_{\text{in}}, \omega_{\text{out}})$ includes the relevant information of this scattering process and contributions from different initial states $|n\rangle$.

$$F_{\text{RIXS}}(\omega_{\text{in}}, \omega_{\text{out}}) = \sum_n F_{\text{RIXS}}^{(n)}(\omega_{\text{in}}, \omega_{\text{out}}) \times \frac{e^{-E_n/k_B T}}{Z} \tag{58}$$

where $e^{-E_n/k_B T}/Z$ is the Boltzmann factor with the partition function Z. The parameters ω_{in} and ω_{out} denote to the absorbed and the emitted photon, respectively. The spectral function for L-edge RIXS is proportional to the L-edge cross section $F_{\text{RIXS}} \propto \frac{\delta^2 \sigma}{\delta \Omega \delta \omega}$ and is given by the Kramers-Heisenberg formula [15, 12, 63]

$$F_{\text{RIXS}}^{(n)}(\omega_{\text{in}}, \omega_{\text{out}}) = \sum_f \left| \langle f | \hat{T}_{\text{E}} G(\omega_{\text{in}}) \hat{T}_{\text{I}} | n \rangle \right|^2 \delta(\omega_{\text{in}} + E_n - \omega_{\text{out}} - E_f) \tag{59}$$

$$= \sum_f \left| \sum_m \frac{\langle f | \hat{T}_{\text{E}} | m \rangle \langle m | \hat{T}_{\text{I}} | n \rangle}{\omega_{\text{in}} + E_n - E_m + i\Gamma_{\text{L}}} \right|^2 \delta(\omega_{\text{in}} + E_n - \omega_{\text{out}} - E_f) \tag{60}$$

$$= \sum_f \left| \langle f | \hat{T}_{\text{E}} \frac{1}{\omega_{\text{in}} + E_n - \hat{H} + i\Gamma_{\text{L}}} \hat{T}_{\text{I}} | n \rangle \right|^2 \delta(\omega_{\text{in}} + E_n - \omega_{\text{out}} - E_f), \tag{61}$$

where the states $|n\rangle$, $|m\rangle$ and $|f\rangle$ represent the initial, intermediate and final states, respectively. The corresponding energies are E_n, E_m and E_f. Γ_{L} is the lifetime width in the intermediate state. $\hat{T}_{\text{I}}$ and $\hat{T}_{\text{E}}$ are the transition operators of the photon absorption and emission in the dipole approximation, respectively. The geometry setting of the RIXS process including the photon polarization is encoded in these operators. The operator $\hat{H}$ is the Hamiltonian of the whole system and replaced by the AIM Hamiltonian $\hat{H}_{\text{AIM}}$ with the DMFT hybridization intensity [22].

4 RIXS Study on High Valence Transition Metal Oxides

This section includes the analysis of our RIXS study of isoelectric cuprates and is based on the publication *"Continuum charge excitations in high-valence transition metal oxides revealed by resonant inelastic X-ray scattering"* by Atsushi Hariki, Mathias Winder, and Jan Kuneš [15]

4.1 Introduction

Resonant inelastic X-ray scattering (RIXS) techniques have rapidly developed in the last decade. A substantial energy-resolution improvement to less than 50 meV by recent experimental progresses [64] has elaborated this technique to a modern probe to study various types of strongly correlated materials. The L-edge threshold ($2p \rightarrow 3d \rightarrow 2p$) is a popular choice to investigate TMO due to its direct involvement of TM $3d$ states in the excitation process. We note that the intermediate state in L-edge RIXS corresponds the final state of L-edge XAS. The RIXS intensity usually depends on the incident X-ray energy ω_{in} sensitively since the overlap of final states and the intermediate state by the X-ray irradiative operator affects the transition probability, see Eq. 60. Thus on the one hand, a proper description of the intermediate states in addition to initial and final states is required to interpret RIXS, but on the other hand, the intermediate state provides a "filter" to measure specific final states of interest in the RIXS spectrum selectively. Typically L-edge RIXS shows two types of behaviors; Raman-like (RL) behavior, showing the signal at a fixed energy loss ω_{loss} with scanning photon energy ω_{in} across the resonance; fluorescence-like (FL) behavior, showing a constant emission energy ω_{out} and thus a linearly dispersive feature as a function of ω_{loss}. The FL behavior occurring in some TM compounds attracted recently much attention and is under an active debate [21, 17, 20].

Bisogni et al. [17] performed an experimental Ni L_3-edge RIXS study for rare earth nicklates (ReNiO$_3$), see Fig. 13. Fig. 13(a:a) represents the L_3-edge XAS spectra with a double peak structure. Figs. 13(a:b,a:c) show the Ni L_3-edge RIXS spectra in metallic and insulating phase, respectively. The abscissa corresponds to the incident photon energy (ω_{in}) whereas the ordinate corresponds to the energy loss (ω_{loss}) of the emitted photon. NdNiO$_3$ shows a linear FL behavior where in the low-ω_{loss} regime the FL feature exhibits distinct temperature dependence connected to the opening of a charge gap (insulating phase) at low temperatures, see Fig. 13(b:c). This confirmed suggestions that NdNiO$_3$ is not a conventional CT insulator with a positive CT energy but instead has a negative CT energy. Within the study of Bisogni et al. the double-peak feature in L_3-XAS is attributed to the atomic-multiplet origin, which seems to conflict with the FL behavior. It is argued that the FL feature arises from the continuum electron-hole pair (EHP) excitation. The FL feature is a signature of unbound particle-hole pairs in the final state of RIXS. In a high-valence system with a small or negative CT energy, which can be reached by self-doping, partially filled O $2p$ bands extending across the Fermi

energy (E_F). This opens an additional pathway for the neutral charge fluctuations, which can be the source of the FL feature.

(a) (a) XAS / (b,c) RIXS spectra

(b) Magnification of the FL gap
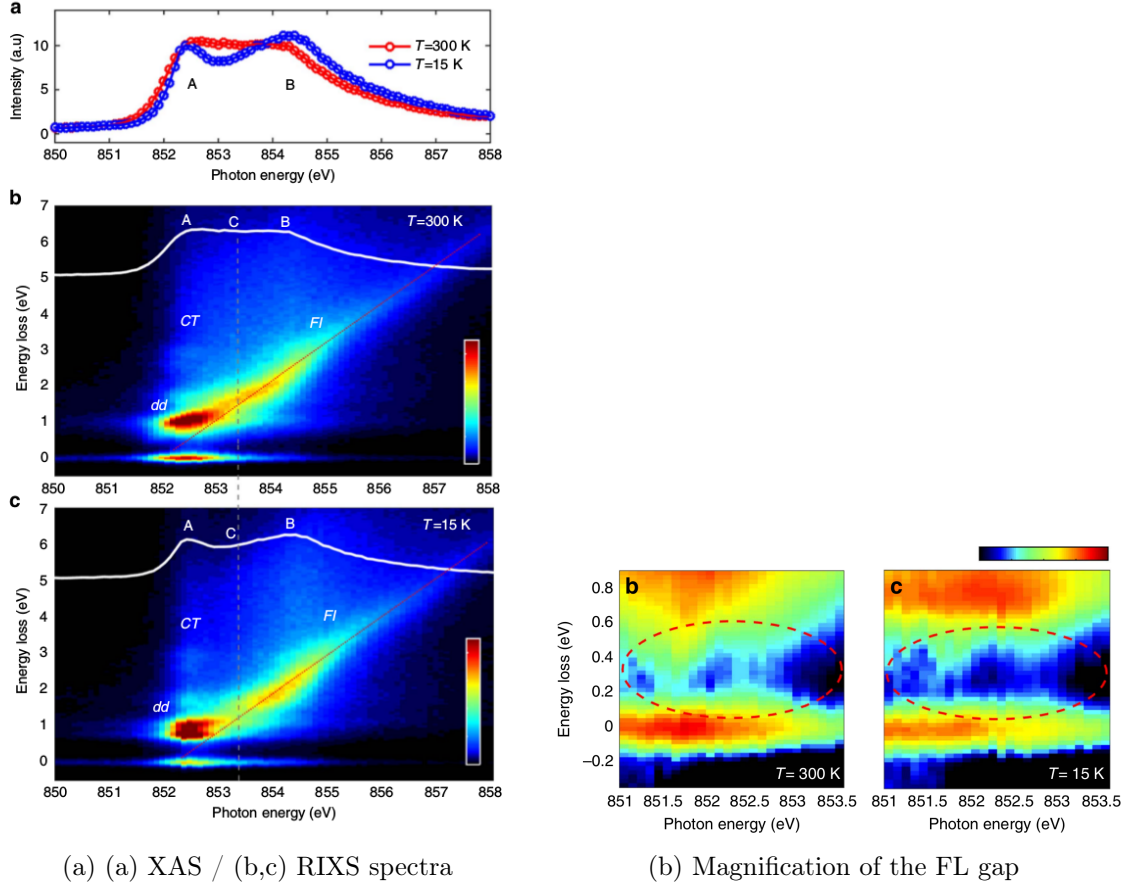
Figure 13: Experimental L_3-edge XAS and RIXS for NdNiO$_3$, adapted from [17]

Another interpretation for the FL feature was introduced by Zhou et al. [20]. They studied L-edge RIXS in LaAlO$_3$/SrTiO$_3$ heterostructures and interpreted the relative intensity of the FL feature as a measure of concentration of itinerant carriers. Pfaff et al. [21] questioned this conclusion recently within their study of Ti $3d$ electrons at the interface of LaAlO$_3$/SrTiO$_3$ heterostructures. Pfaff et al. showed that the amount of localized and itinerant Ti $3d$ electrons in the ground state do not scale with the intensities of the RL and FL peaks. They suggested therefore that either RL or FL features reflect the nature of the intermediate state of the RIXS process. We can confirm the suggestions of Pfaff et al. within our study.

Bisogni et al. [17] have opened opportunities to do further studies of negative CT systems by L-edge RIXS. We build on this study and try to answer following open questions:

(i): how does the continuum electron-hole pair excitation with the O $2p$ character acquire a strong resonance across TM L-edge

(ii): how do the RIXS spectra develop with a CT-energy decrease, which could accompany a collapse of the Mott gap and/or intervention of the O $2p$ states to the low-energy excitations

(iii): which theoretical model, cluster, AIM with modeled bath or AIM with LDA+DMFT bath, can be employed in the analysis and which one gives a proper quantitative and qualitative description of the spectra

We perform a L_3-edge RIXS study for $LaCuO_3$ and $NaCuO_2$ within this thesis. We have chosen cuprates, instead of nickelates as in the study of Bisogni et al. [17], due to well known electronic structure. The theoretical description of spectra consists of two steps. First the determination of the ground state or the thermal equilibrium and then the evaluation of the excitations. The ground state for the cuprates is well known, whereas the ground state of nickelates is a subject of an active debate. We focus on the evaluation of the excitations.

4.2 Crystal Structure of $LaCuO_3$ and $NaCuO_2$

We analyze in the following the crystal structure of isoelectronic Cu^{3+} compounds $LaCuO_3$ and $NaCuO_2$. We have chosen these cuprates as model systems of high-valence transition metal oxides for our L_3-edge RIXS study. Both share a small CT energy [65, 11, 66, 67, 68] which leads to a small or no gap in the band structure near the Fermi energy E_F [65, 66, 67, 69, 70]. By tuning the CT energy from the positive to the negative regime, the system changes from insulator to metal. As we see later, the key difference between the two compounds is the lattice geometry. $LaCuO_3$ has a corner-sharing CuO_6 octahedra geometry, whereas the geometry of $NaCuO_2$ consists of edge-sharing CuO_4 plaquettes, see Fig. 14. For $LaCuO_3$ we review the paramagnetic metal (PM) and the antiferromagnetic insulating (AFI) phases, reflecting the unclear experimental situation [66, 67, 69, 70]. For $NaCuO_2$ we review the paramagnetic phase.
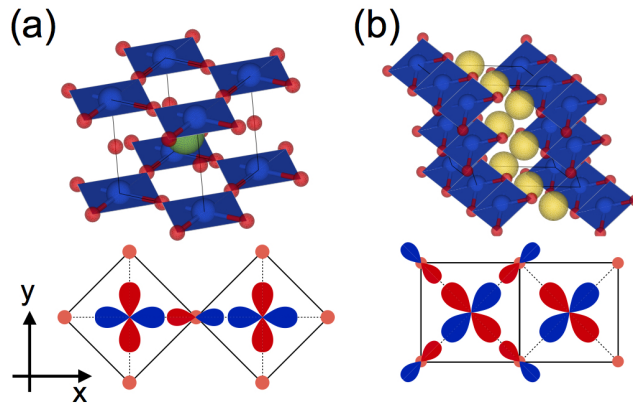
Figure 14: The crystal structure of (a) $LaCuO_3$ and (b) $NaCuO_2$ visualized by VESTA [71]. The blue, red and green, yellow circles represent Cu, O, La and Na atoms, respectively. The sketch of the xy plane is shown together. Adapted from [15]

Fig. 14 shows the crystal structures of the studied cuprates. $LaCuO_3$ has a tetragonal structure with a corner-sharing overlap in the xy-plane of Cu $3d_{x^2-y^2}$ and the O p_x / p_y orbitals, see Fig. 14(a). $NaCuO_2$ has a monoclinic structure and a edge-sharing Cu $3d_{xy}$ with O $2p$ orbitals. The LDA calculation is performed using the WIEN2K [53] package in $P4/m$ tetragonal structure for $LaCuO_3$ and C2/m monoclinic structure for $NaCuO_2$, see Fig. 14. The LDA bands of Cu $3d$ are mapped onto a dp model using the codes WIEN2WANNIER [48] and WANNIER90 [47].
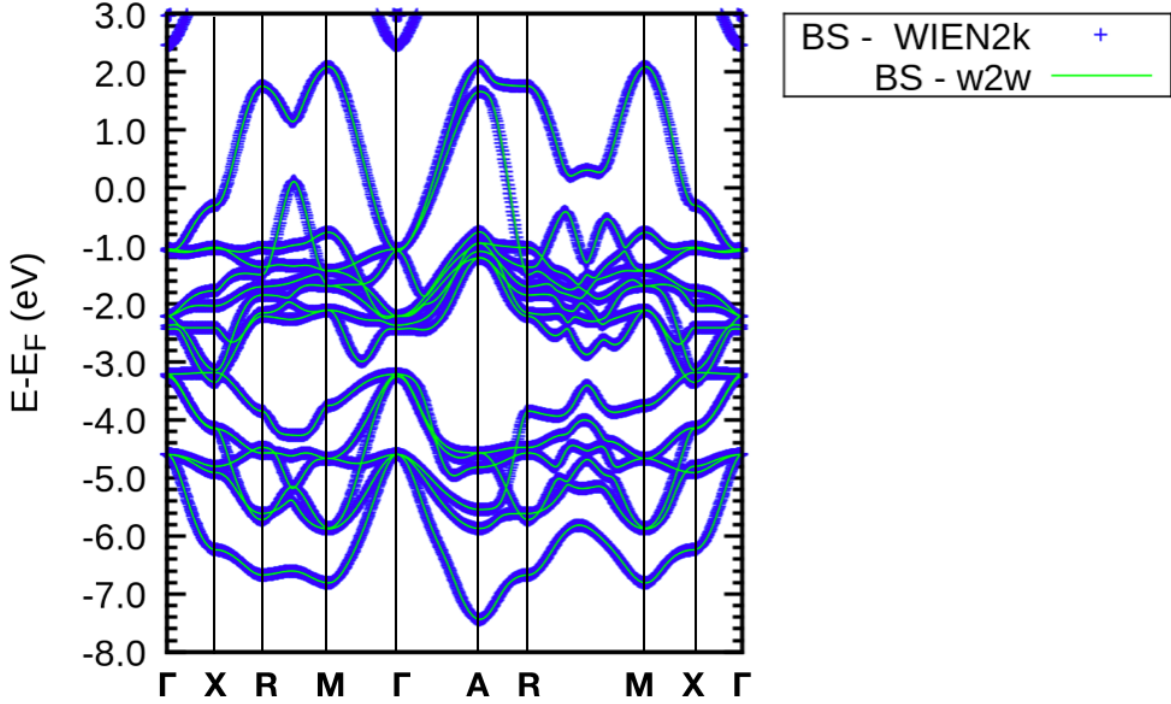
Figure 15: Comparison between band structure of $LaCuO_3$ calculated with WIEN2k [53] and the tools WIEN2WANNIER [48] and wannier90 [47]; plotted with gnuplot [72]

Fig. 15 shows the band structure of $LaCuO_3$ in the energy window of $(-8 \sim -2$ eV$)$. The abscissa shows various k-points from the first Brillouin zone. We see here a comparison between the by LDA (blue) and the by Wannier functions (green) calculated band structure. Both band structures coincide. The nine O $2p$ bands lie below the Fermi level $(-7 \sim -1$ eV$)$, whereas the five valence bands, d_{e_g} and $d_{t_{2g}}$, are close to the Fermi energy $(-2 \sim 2$ eV$)$. The LDA calculation shows a metallic phase of $LaCuO_3$ due to the crossing of Fermi energy by the Cu d_{e_g} bands. We use the band structure, generated by the wannierization, and the Hamiltonian, provided by wannier90 [47], to construct the dp model.

4.3 Computational Aspects of LDA, DMFT and Spectral Calculations

In the following we review the applied parameters of (i) the dp model Hamiltonian $\hat{H}_{dp}$, see Eq. 18, (ii) the AIM Hamiltonian $\hat{H}_{\mathrm{AIM}}$, see Eq. 23, and the computational aspects (iii) of the spectral calculations, see Eqs. 53,59.

(i): The on-site energies $\varepsilon_d(\gamma)$, $\varepsilon_p(\lambda)$ and the hopping amplitudes t_{pd}, t_{dd}, t_{pp} are provided by the wannier90 [47] code. The on-site Coulomb interaction U_i^{int} in Eq. 18 can be approximated by the density-density form. We use the parameters $U = 7.5$ eV and $J = 0.98$ eV, which are typical values for Cu systems.

(ii): The Cu $3d$ on-site energies $\varepsilon_d(\gamma) \rightarrow \varepsilon_d(\gamma) - \mu_{\mathrm{dc}}$ are the energies of the Wannier states $\varepsilon_d(\gamma)$. These states are shifted by the double-counting correction μ_{dc}. The double-counting term μ_{dc} corrects the electronic correlation already included in the LDA calculation. The μ_{dc} renormalizes the p–d splitting and thus relates to the charge transfer energy. An increase of the double-counting energy reduces the CT energy. We treat μ_{dc} as adjustable parameter and determine μ_{dc} by comparing the calculated spectra with experimental L-edge XAS and valence XPS spectra. Therefore we performed several calculations with various μ_{dc} values. For the monopole part of the core-hole potential term, we employed U_{dc}=8.5 eV. The SO coupling within the $2p$ shell and the anisotropic part of the $2p$–$3d$ interaction (defined by the parameters F^k, G^k, see Ch. 3.4.1) are calculated with an atomic Hartree-Fock code. We scaled the F^k and G^k values down to 85% to simulate the effect of intra-atomic configuration interaction from higher basis configurations which are neglected in the atomic calculation. This is a successful treatment in L-edge XAS and RIXS analysis for TMO [12, 73, 74, 75]. Within the DMFT cycle we use as an impurity solver the continuous-time quantum Monte Carlo method, see Ch. 3.4.2.

(iii): The computationally demanding spectral calculations, as well as the DMFT calculations, were performed on the Vienna scientific cluster VSC-3 [76]. We used one node with an 8-core Intel CPU with 128 GB RAM. We combined the RIXS with preliminary XAS studies. Combining these two spectroscopic methods gains advantages e.g. the physical understanding of the intermediate RIXS state, which is the final state in XAS and the reduction of expensive calculation costs due to the preliminary XAS scan. An XAS calculation for the studied cuprates needs about 2 hours computation time. For the RIXS calculation, we defined an energy mesh for the incident photon energy in steps of 0.1 eV over the Cu L_3-edge. The computation time of the RIXS spectra depends heavily on the mesh of incident photon energies. For the reported calculations the computation time was about 60 hours for 100 discrete incident photon energies.

For the calculation of both spectral functions F_{XAS}, see Eq. 53, and F_{RIXS}, see Eq. 59, we employed the CI scheme with discretized bath-states. Each bath consists of 25 discrete levels per spin and orbital. The initial state is computed using the Lanczos method with a convergence within around 200 steps. The intermediate state propagated by the resolvent as $(\omega_{\mathrm{in}} + E_n - \hat{H} + i\Gamma_{\mathrm{L}})^{-1}\hat{T}_{\mathrm{I}}|n\rangle$ is computed using the conjugate-gradient method. The lifetime width Γ_{L} in the intermediate state is set to a constant value of 0.3 eV. The overlap to the final states in RIXS are computed again using the Lanczos

method. The convergence is similar to the initial state and is reached within 200 steps.

4.4 LDA+DMFT Analysis: Valence spectrum and Hybridization

We analyze below the results of the LDA+DMFT calculations for $LaCuO_3$ in paramagnetic metallic (PM) and antiferromagnetic insulating (AFI) phase and $NaCuO_2$ in paramagnetic phase. The partial density of states (PDOS), also called one-particle spectral function, and the hybridization spectra for different double counting energies μ_{dc} are important to discuss the physical response of the system. Furthermore we determine the configuration weights of the ground state which are dependent on the double counting energies. With these we define a proper basis configuration which is applied within the CI scheme to calculate the spectral functions, see Ch. 3.5.
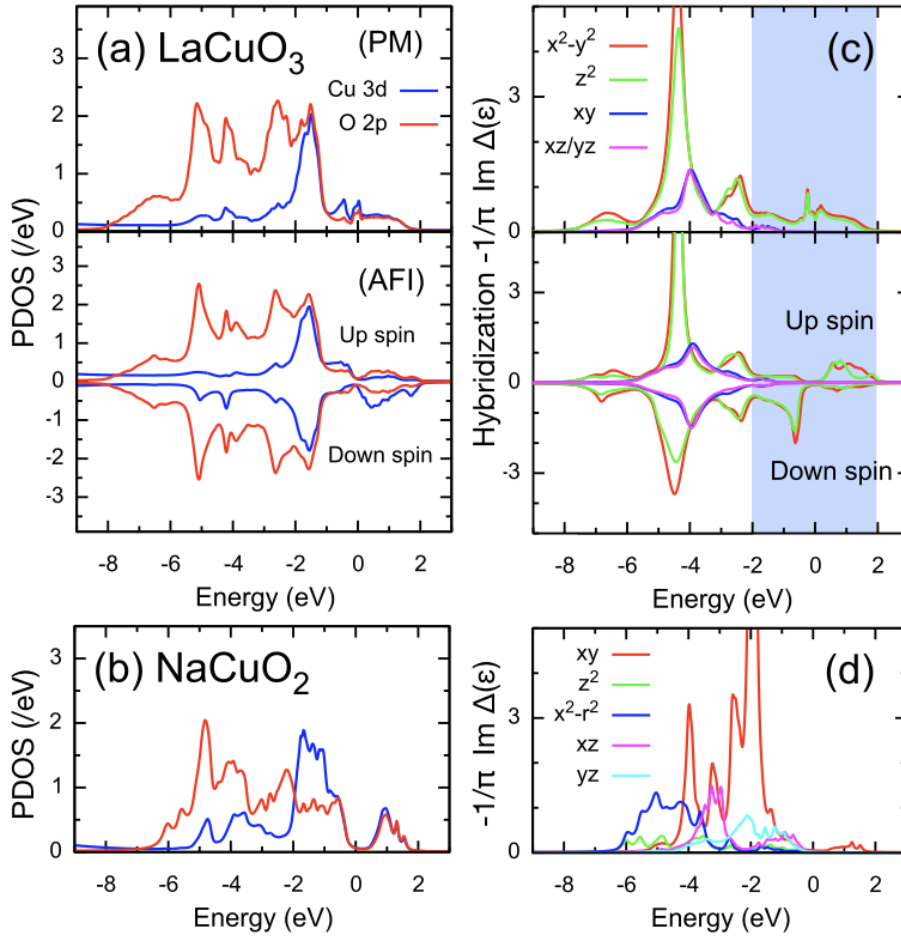
Figure 16: LDA+DMFT PDOS of (a) $LaCuO_3$ in the PM and AFI phases and (b) $NaCuO_2$. The hybridization function of (c) $LaCuO_3$ in the PM and AFI phases and (d) $NaCuO_2$. The energy origin is taken at E_F. Adapted from [15]

Figs. 16(a,b) show the by LDA+DMFT calculated one-particle spectral functions of $LaCuO_3$ and $NaCuO_2$. We use here a double-counting energy of $\mu_{dc}=56.64\pm1$ eV which

corresponds to the zero or negative charge transfer regime. The results calculated with μ_{dc}=56.64±1 eV are consistent with earlier valence and Cu L-edge XAS studies [65, 66]. The solutions of LaCuO$_3$ in paramagnetic metal (PM) and antiferromagnetic insulator (AFI) phases can also be determined with LDA+U calculations [67]. The band-insulator character of NaCuO$_2$ with a gap ($E_{gap} \approx 0.5$ eV) is already present in the LDA calculation [77, 78]. The spectral functions suggest an existing phase space for a continuum of p–p excitations in the few eV range.

Figs. 16(c,d) show the hybridization $\Delta(\varepsilon)$ of the $3d$ bands with the bath for (c) LaCuO$_3$ and (d) NaCuO$_2$. Within the red region of Fig. 16(c) LaCuO$_3$ exhibits a broad hybridization intensity with a large hybridization for $d_{x^2-y^2}$ and d_{z^2} bands with the bath. The up-spin components in the antiferromagnetic insulating phase have a stronger intensity, with a peak at around -4 eV, than the low-spin components. In the blue region of Fig. 16(c) the $d_{x^2-y^2}$ and d_{z^2} bands are still dominant but the hybridization is broad without clear peaks at certain energies. Just the down-spin hybridization of the antiferromagnetic insulating phase dominates below the Fermi energy ($E_F = 0$ eV) whereas the up-spin component dominates above the Fermi energy. NaCuO$_2$ shows a large hybridization intensity only below the Fermi energy and shows a sharp peak feature for the d_{xy} hybridization. The sharp peak reflects the hybridization to the in the lattice neighboring O $2p$ molecular states, the σ-bonding states.
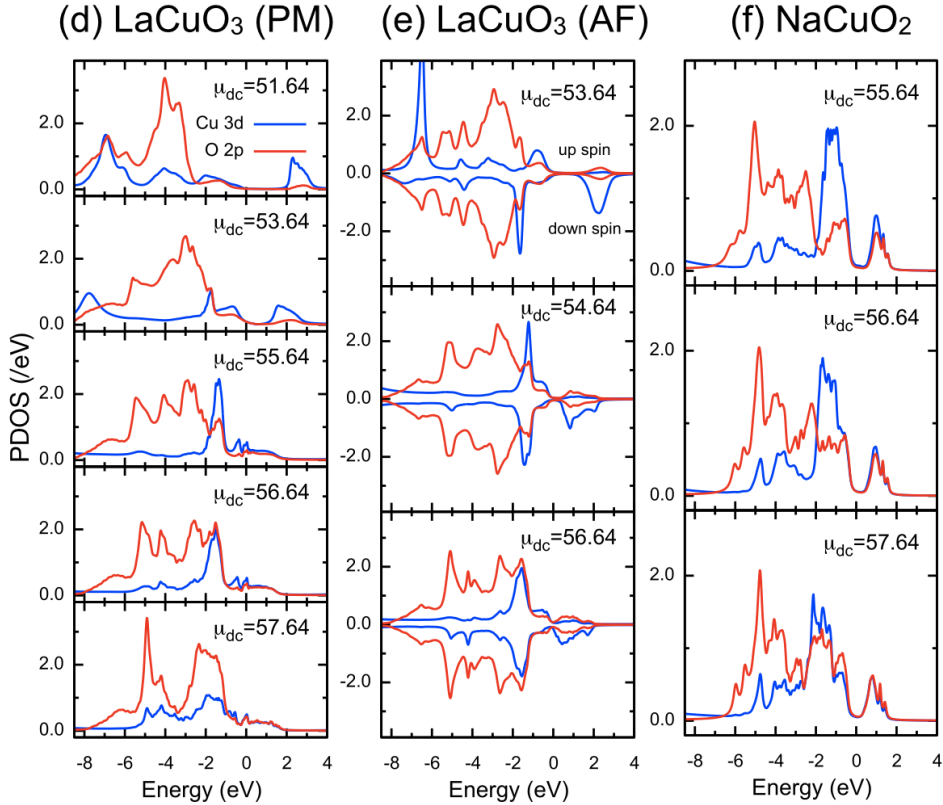
Figure 17: Calculated PDOS of (d) LaCuO$_3$ (PM), (e) LaCuO$_3$ (AF), and (f) NaCuO$_2$, adapted from the supplementary materials of [15].

38

Fig. 17 shows the by DMFT calculated PDOS for different double-counting energies μ_{dc} in LaCuO$_3$ and NaCuO$_2$. Small double counting energies in LaCuO$_3$ (PM), see Fig. 17(d), and LaCuO$_3$ (AF), see Fig. 17(e), exhibit an insulating phase compared to the band structure of the LDA calculation, see Fig. 15, where the bands cross the Fermi energy and therefore LaCuO$_3$ exhibit a metallic phase. $\mu_{dc} = 56.64$ corresponds to a CT energy $\Delta = 0$ eV. Values below $\mu_{dc} < 56.64$ corresponds to the positive CT regime whereas $\mu_{dc} > 56.64$ marks the negative CT regime. For $\mu_{dc} > 55.64$ the gap at Fermi-level closes and a metal phase results. The valence spectra with $\mu_{dc} = 56.64 \pm 1$ eV give a reasonable agreement to early photoemission data [68, 66]. The TM compound NaCuO$_2$, showed in Fig. 17 keeps its insulating phase for the double counting energies within the regime of $\mu_{dc} = 55.64 \sim 57.64$ eV. Fig. 18 shows the hybridization intensities for different double counting values.
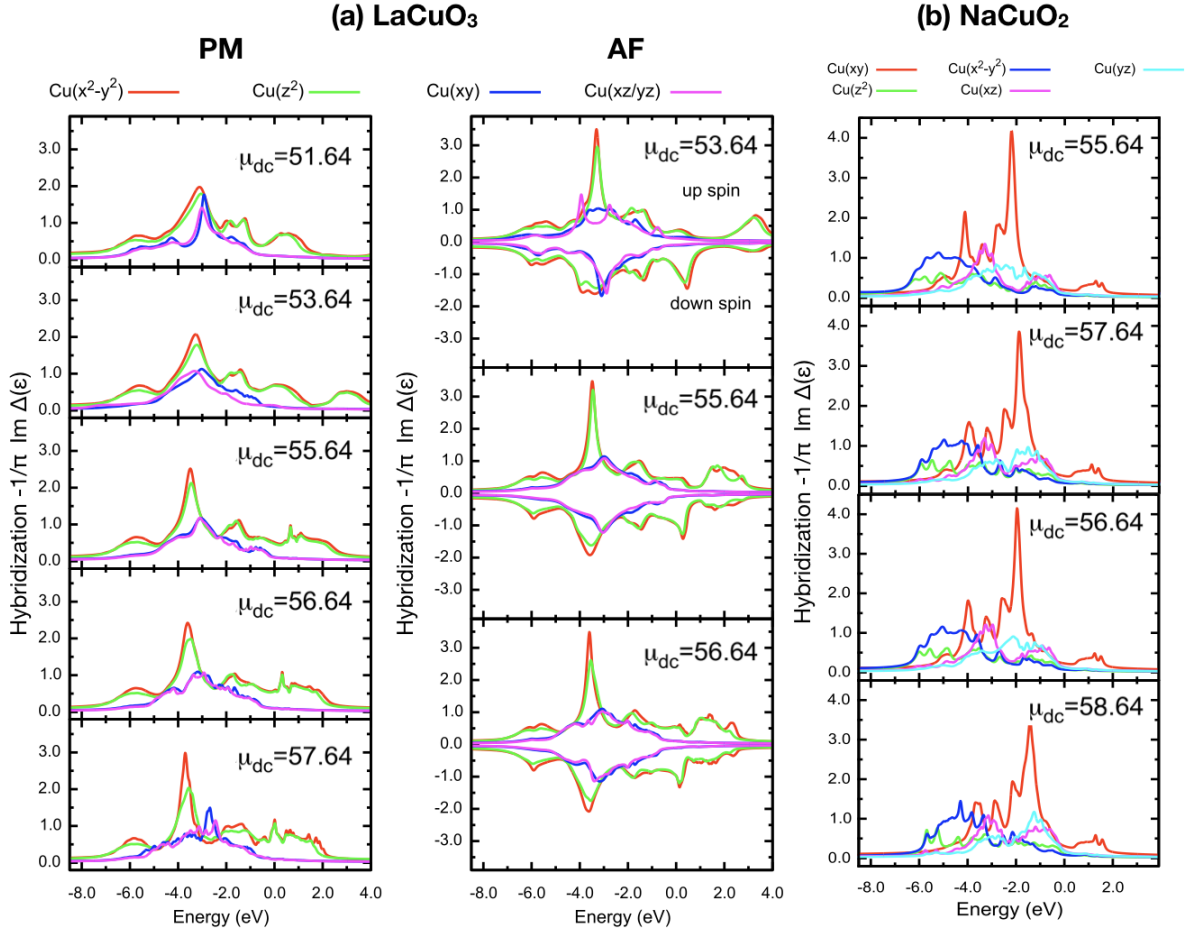
Figure 18: Calculated hybridization spectra of (a) LaCuO$_3$ (PM/AF) and (b) NaCuO$_2$.

Fig. 18(a) shows the hybridization intensity for LaCuO$_3$. The O $2p$ states have a large hybridization intensity below the energy -2.0 eV as well as the mixed states of O $2p$ and Cu $3d$ on the valence top in the energy window $-2 \sim 2$ eV. The spin dependence in the AF ordering becomes weaker with an increase of μ_{dc}. The sharp peaks of the Cu

d_{xy} hybridization remain for NaCuO$_2$, see Fig. 18(b).

For the calculation of the spectral functions with the CI scheme we analyze the configuration weights of the initial state in the thermal equilibrium depending for different double counting energies μ_{dc}, see Fig. 19.
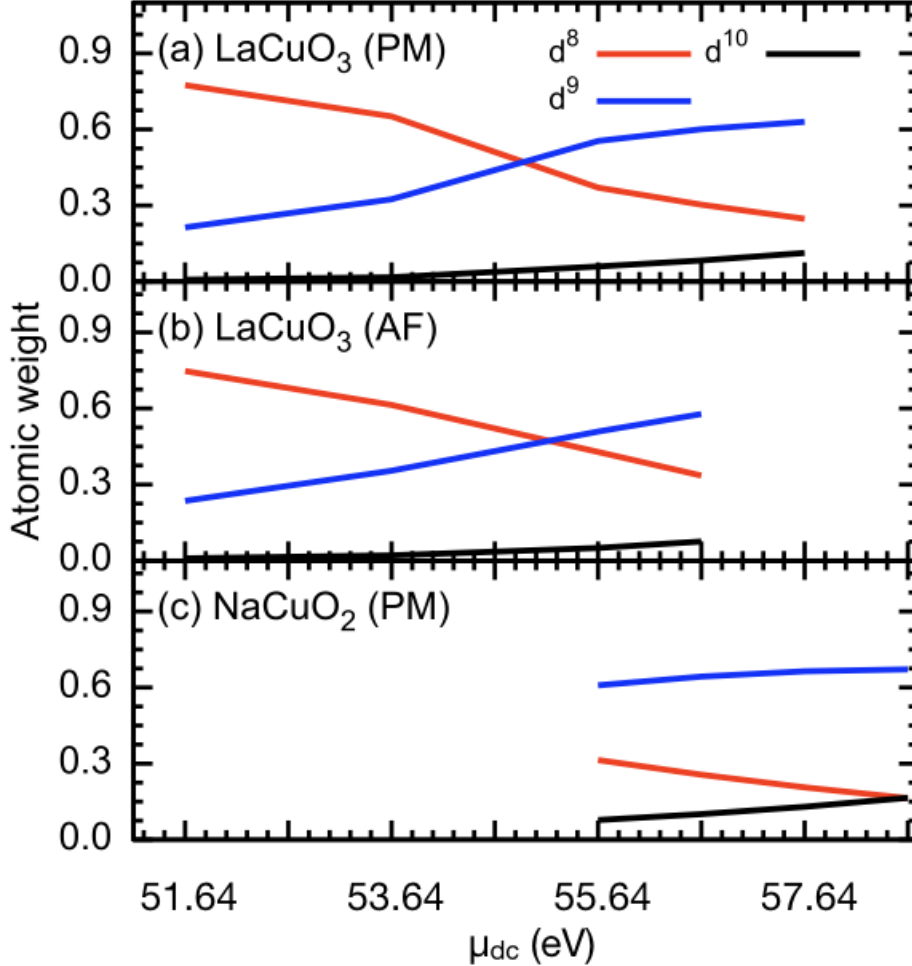
Figure 19: Calculated configuration weights of (a) LaCuO$_3$ (PM), (b) LaCuO$_3$ (AF), and (c) NaCuO$_2$

For LaCuO$_3$ in PM phase, see Fig. 19(a), the configuration weight of $|d^9\rangle$ becomes for a double counting energy $\mu_{dc} < 55$ eV dominant, whereas for $\mu_{dc} > 55$ eV the state $|d^8\rangle$ dominates. The configuration weights within the AF phase in Fig. 19(b) have a similar behavior as in the PM phase. Fig. 19(c) shows the weights within the PM phase of NaCuO$_2$, where $|d^9\rangle$ dominates for all calculated double counting energies. The weight of $|d^{10}\rangle$ is for both cuprates very weak and is almost zero for double counting energies $\mu_{dc} < 53.5$ eV.

4.5 LDA+DMFT Analysis: XAS and RIXS

We compute L_3-edge RIXS of LaCuO$_3$ and NaCuO$_2$ for different double counting energies. We compare the results of the AIM with an LDA+DMFT bath with the cluster model and the AIM with a modeled bath. The modeled bath has a semi-elliptical shape and is in the energy range of the O $2p$ DOS with a width of approximately 4 eV. As already mentioned the intermediate state provides important information for the understanding of the RIXS spectra, thus we discuss the XAS spectra below.
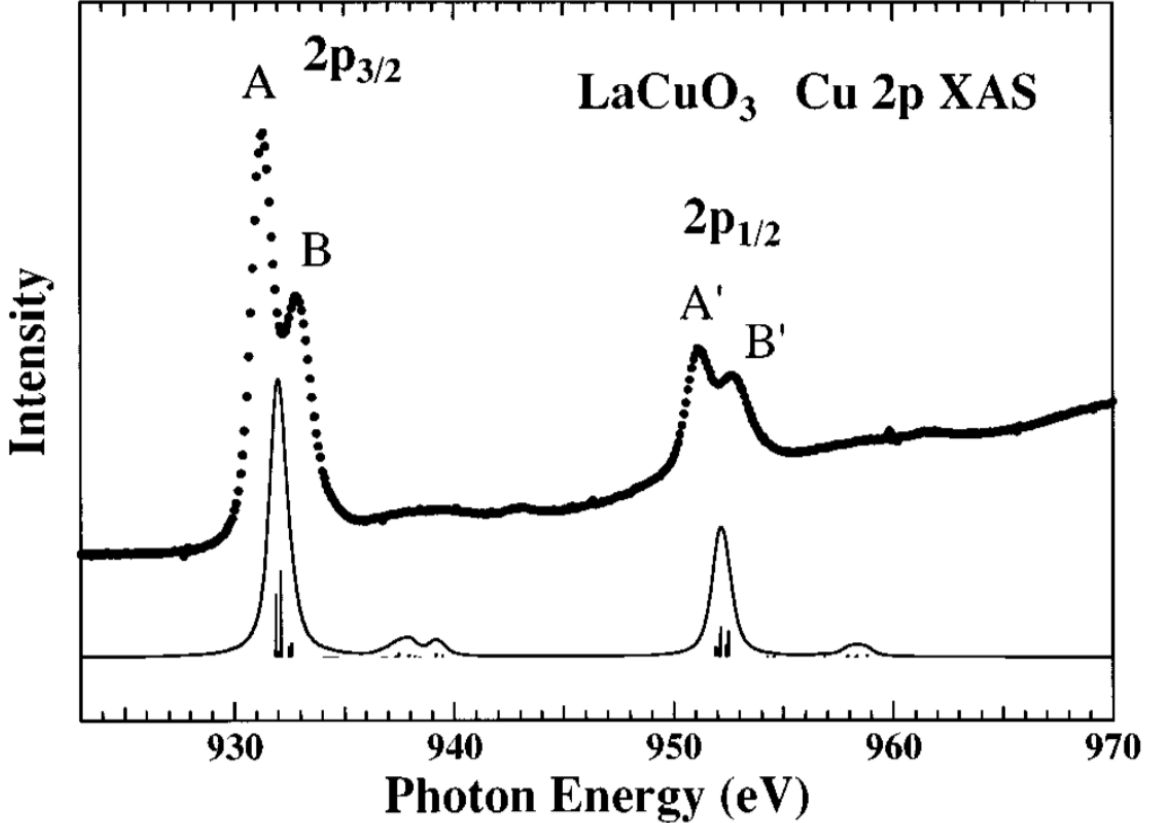
Figure 20: Cu 2p XAS spectrum of LaCuO$_3$ (dots) compared with a cluster model calculation (solid curve), from [66]

Mizokawa et al. [66] performed an experimental Cu $2p$ XAS study for LaCuO$_3$, see Fig. 20. We see a comparison between the experimental spectrum and the corresponding cluster model calculation. The spectrum consists of the $2p_{3/2}$ main peak (A) at $\sim$ 931 eV, also called L_3-edge, and the $2p_{1/2}$ main peak (A') at $\sim$ 951 eV, also called L_2-edge. The shoulders (B) and (B') are missing in the calculations of the CuO$_6$ cluster model [66, 79], indicating that the shoulders are not of d–d or CT origin but due to a final state delocalized beyond the CuO$_6$ cluster. Such a nonlocal charge excitation is captured by the present approach [22] and also in our actual study of the Cu $2p$ XAS, see Fig. 21(a).

41
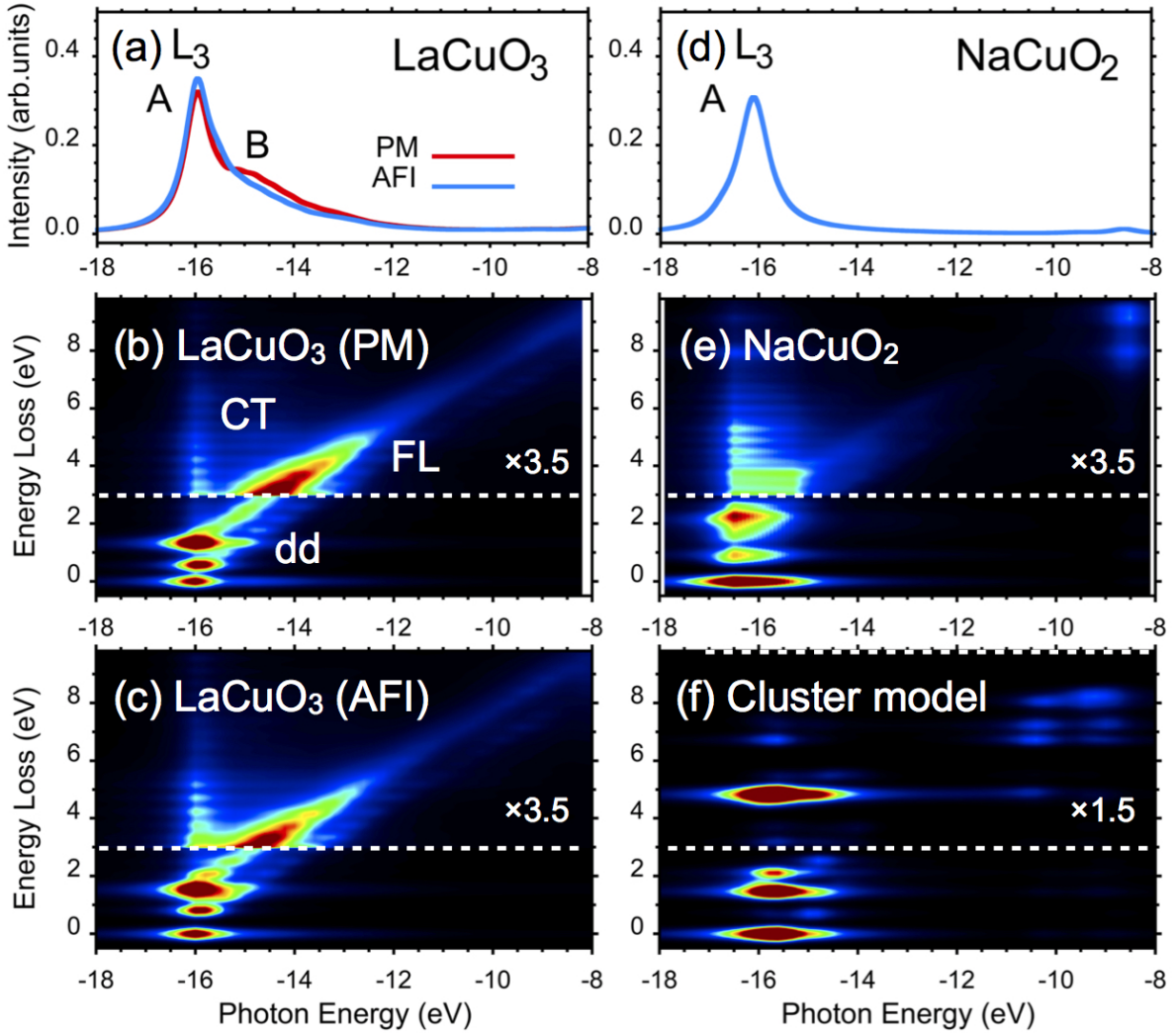
Figure 21: (a)-(e) the calculated L-edge XAS and RIXS for $LaCuO_3$ in PM and AFI phase (left) and $NaCuO_2$ (right). The RIXS intensity with $\omega_{loss} \geq$ 3.0 eV (dashed line) are magnified by 3.5 times. (f) the calculated RIXS by the CuO_6 cluster model. The spectral broadening is considered using a Gaussian of 150 meV for RIXS and a Lorentzian 300 meV for XAS (HWHM). Adapted from [15]

The XAS spectra in Figs. 21(a,d) are shifted by a constant energy of 947 eV compared to the XAS spectrum in Fig. 20. The $2p$ XAS spectrum of $NaCuO_2$ shows a single-peak (A) at -16 eV, while that of $LaCuO_3$ shows an additional shoulder (B). This shoulder is enhanced in PM phase and is also observed in the experiment, see Fig. 20.

Figs. 21 (b,c,e,f) show the L_3-edge Cu $2p$ RIXS spectra of $LaCuO_3$ and $NaCuO_2$. We used for the calculations polarized photons, see Ch. 3.5.3. For $LaCuO_3$ the scattering plane is in the xy-plane whereas for $NaCuO_2$ the scattering plane is 45°-rotated along the z-axis compared to the xy-plane in Fig. 14(b).

The RIXS spectra of $NaCuO_2$ and $LaCuO_3$ differ from each other. When we tune ω_{in}

to the peak (A) of XAS we see two distinct d–d transitions with a RL behavior. This is similar to the Cu^{3+} material $Zn_{1-x}Cu_xO$ [80]. At higher ω_{in} the RIXS of LaCuO$_3$ shows a linear FL feature. There is just a minor difference between the AFI and PM phase. For NaCuO$_2$ the FL feature is suppressed and is similar to the spectrum of the cluster model calculation, see Fig. 21(f). The outcomes for different double counting energies are presented in Fig. 22.
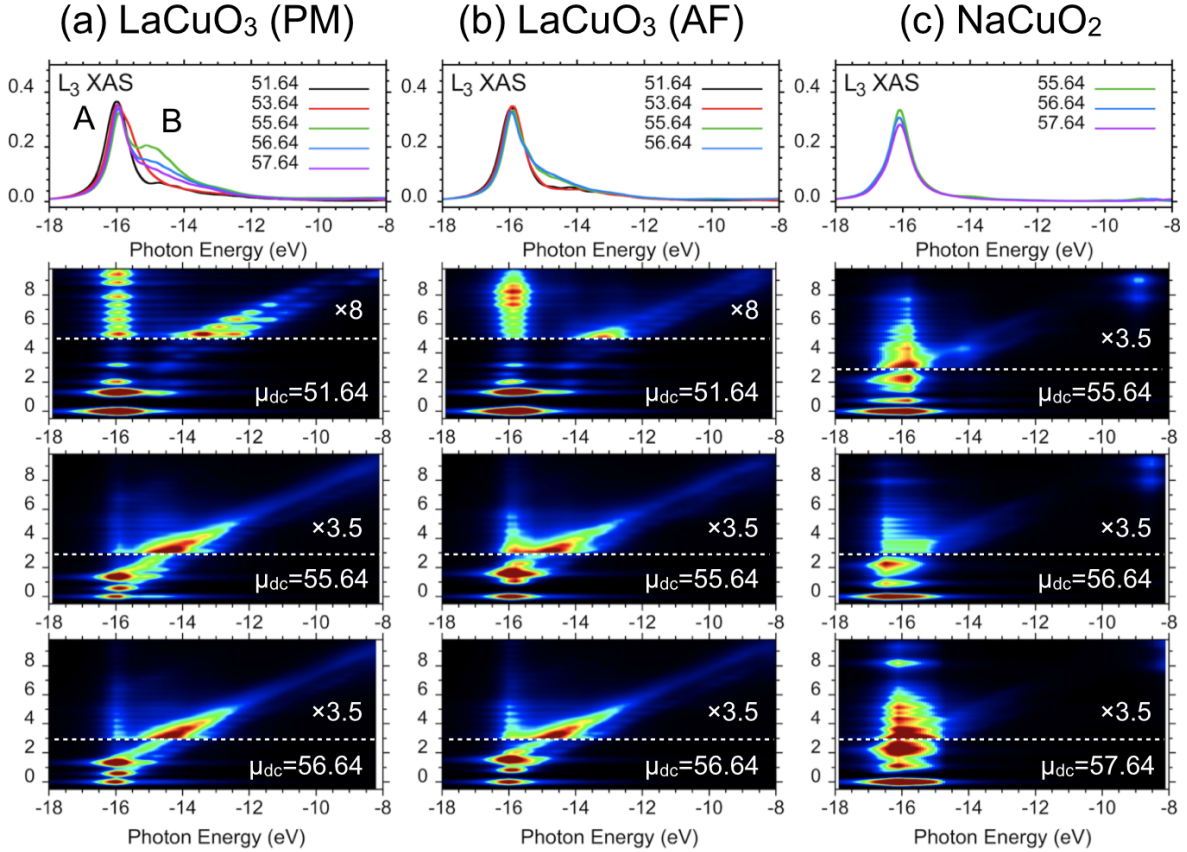
Figure 22: Calculated L_3-edge XAS and RIXS for (a) LaCuO$_3$ (PM), (b) LaCuO$_3$ (AF), and (c) NaCuO$_2$, adapted from the supplementary material of [15]

The XAS spectra of LaCuO$_3$, displayed in Figs. 22(a,b), show a sharp peak (A) at around -16 eV for all double counting energies. For μ_{dc}=51.64 eV the XAS spectra correspond to be deep in the Mott insulating phase and show a weak multiplet feature at around -15 eV. This is similar to the Ni L-edge XAS of NiO with $3d^8$ electronic configuration [81]. With an increase of μ_{dc} a new shoulder (B) evolves in both phases. The metal-insulator transition occurs for the PM phase at $\mu_{dc} \sim$55.64 eV, whereas for the AF phase the gap doesn't close. The XAS spectra for μ_{dc}=56.64±1 eV match with present XAS data measured by using the total electron yield method [66]. The XAS spectra of NaCuO$_2$ show a weaker μ_{dc} dependence. The shoulder (B) is not present, which is consistent with experiments [82].

The RIXS spectra of LaCuO$_3$, see Figs. 22(a,b), show coexisting FL and RL features when scanning ω_{in} across the L_3 main line. For small double counting energies, e.g. μ_{dc}=51.64 eV, the FL feature appears above the L_3 main line, similar to NiO [83]. The FL feature for higher double counting energies begins at the L_3 main line. The FL feature is absent in RIXS spectra of NaCuO$_2$, see Fig. 22(c), for all calculated double counting energies. In the following we show the RIXS spectra calculated with conventional models.
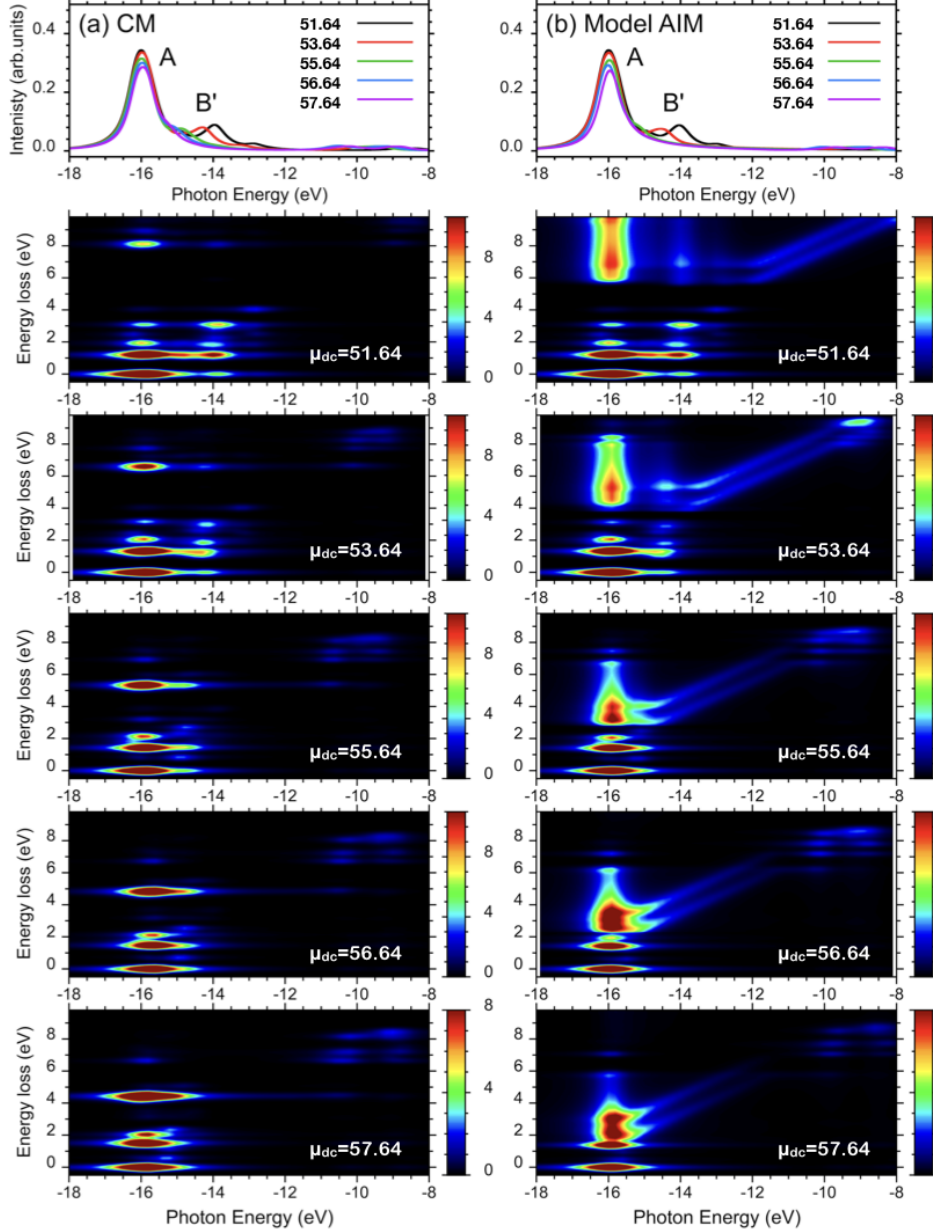
Figure 23: Calculated L_3-edge XAS and RIXS for LaCuO$_3$ (PM) (a) Cluster model, (b) Anderson with semi-elliptical bath in the energy window of the O $2p$ DOS

Fig. 23 shows the L_3-edge XAS and RIXS spectra for $LaCuO_3$ in the paramagnetic phase calculated for the cluster model and for AIM with a semi-elliptical bath for different μ_{dc} energies. We see a clear difference in the XAS spectra at peak (A) compared to the spectra in Fig. 22(a). The shoulder (B), see Fig. 21(a), is suppressed, instead we see a shoulder (B') which arises from the multiplet structure of the Cu $2p$ states. The FL feature is missing in the cluster model calculation, whereas the Anderson impurity model with the semi-elliptical bath gives a FL feature.

4.6 Discussion

The calculated RIXS spectra of $LaCuO_3$ are similar to the experimental observations in $NdNiO_3$ [17]. The FL feature in $LaCuO_3$ can be explained by the continuum of unbound particle-hole pairs mentioned in [17], whereas the missing FL behavior in $NaCuO_2$ has to be discussed in detail.

The absence of RIXS-visible particle-hole excitations at ω_{loss} in the $3 \sim 4$ eV range (FL feature) in $NaCuO_2$ cannot be explained by the small gap in the one-particle spectra, see Fig. 16(b). The FL feature is only affected by the gap opening at low ω_{loss}, see Fig. 24. The density of states, considered in the spectral function of $NaCuO_2$, has a higher intensity above and below the gap than that of $LaCuO_3$, see Figs. 16(a,b). This suggests a larger phase space for particle-hole excitations in $NaCuO_2$.
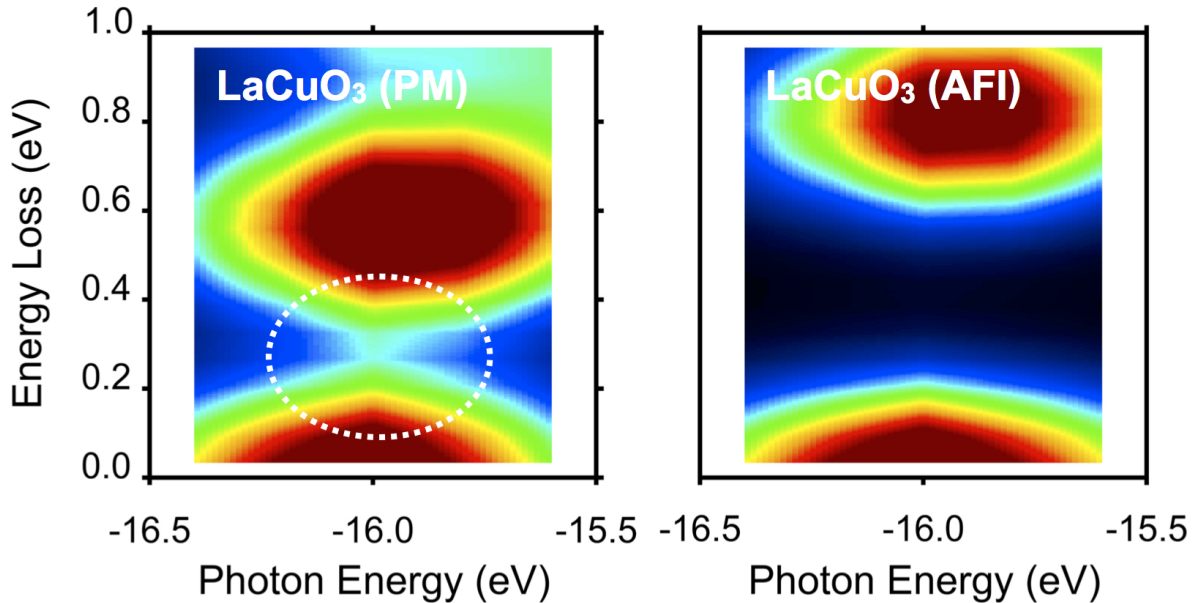
Figure 24: Magnification of the low energy loss region (< 1.0) of RIXS map in PM and AFI phases of $LaCuO_3$. The FL feature continues to zero energy loss ω_{loss} in the PM phase. Adapted from [15]

To explain the missing FL feature in $NaCuO_2$ we analyze the hybridization spectra in Figs. 16(c,d), calculated by the hybridization function $\Delta(\varepsilon)$, see Eq. 42. The hybridization function describes the hybridization of a given Cu atom orbital with the rest of the

crystal, where v_α is the hopping amplitude between the Cu ion and auxiliary states at energies ε_α. We drop here the orbital index γ for simplicity. For instructive reasons we consider first $\Delta(\varepsilon)$ as the hybridization intensity of the cluster model. The hybridization is then a single Dirac δ-function peak at the energy ε_p of the ligand states. The O $2p$ spectral function exhibits two peaks which correspond to the bonding and anti-bonding states.

The hybridization to the nearest-neighbor ligands induces a peak in $\Delta(\varepsilon)$ for e_g orbitals of LaCuO$_3$ and NaCuO$_2$, see Figs. 16(c,d). The continuum part of $\Delta(\varepsilon)$ is strikingly different within the two cuprates. The hybridization intensity in LaCuO$_3$ exists in the low-energy region of -2 to 2 eV, marked as blue region in the figure, whereas for NaCuO$_2$ the intensity is almost not existing, comparable to cluster model. The hybridization function $\Delta(\varepsilon)$ contains information about bonding and the lattice geometry. The lattice geometry, discussed in Ch. 4.2, implies that for LaCuO$_3$ the corner-sharing network of CuO$_6$ octahedra allows electrons (holes) to propagate through the strong Cu-O σ-bonds. This gives a rise to the intensity of the continuum region of $\Delta(\varepsilon)$. The edge-sharing CuO$_4$ plaquettes of NaCuO$_2$ prevent the electron (holes) to propagate through the Cu-O σ-bonds, which are in this structure between Cu ions and orthogonal O $2p$ orbitals. Thus, the crystal resembles a collection of weakly coupled CuO$_4$ clusters.

Furthermore we discuss the influence of the hybridization intensity on the RIXS spectra. In principle all intermediate states which are accessible in XAS contribute to the RIXS process, see Eq. 60. As an estimation, we assume that the intermediate states with an approximately conserved energy in the partial XAS process $|E_m - E_n - \omega_{\text{in}}| \lesssim \Gamma_{\text{L}}$ dominate, while those outside this range cancel approximately out. This can be assumed due to the varying sign of the denominator, but cannot be directly confirmed with the resolvent formulation of Eq. 61. This assumption is supported by the diagonal shape of the FL feature in the ω_{in}-ω_{loss} plane. The diagonal shape suggests that a narrow range of intermediate states are 'excited' that 'decay' into a narrow range of final states with matching the electron-hole excitation. The small intensity for $\varepsilon > 0$ in NaCuO$_2$ implies that the intermediate states with different numbers of conduction electrons hybridize only weakly with another. Consider a RIXS process, schematically written as [15]

$$d^8 + d^9 \underline{L} \rightarrow \underline{c}d^{10}\underline{L} + \underline{c}d^9\underline{L}c' \rightarrow d^8\underline{L}c', \tag{62}$$

where $\underline{c}$, $\underline{L}$ correspond to a hole in $2p$ core-level and in the valence bands, respectively. c' corresponds to an electron in the conduction band. Here the final state is similar to the ground state but has an additional electron hole pair in the continuum, see Fig. 25(d). This process is suppressed in NaCuO$_2$ due to the weak hybridization of states of the type $\underline{c}d^{10}\underline{L}$ and $\underline{c}d^9\underline{L}c'$. A hole transferred from Cu to O in NaCuO$_2$ has a small probability to escape the CuO$_4$ cluster.
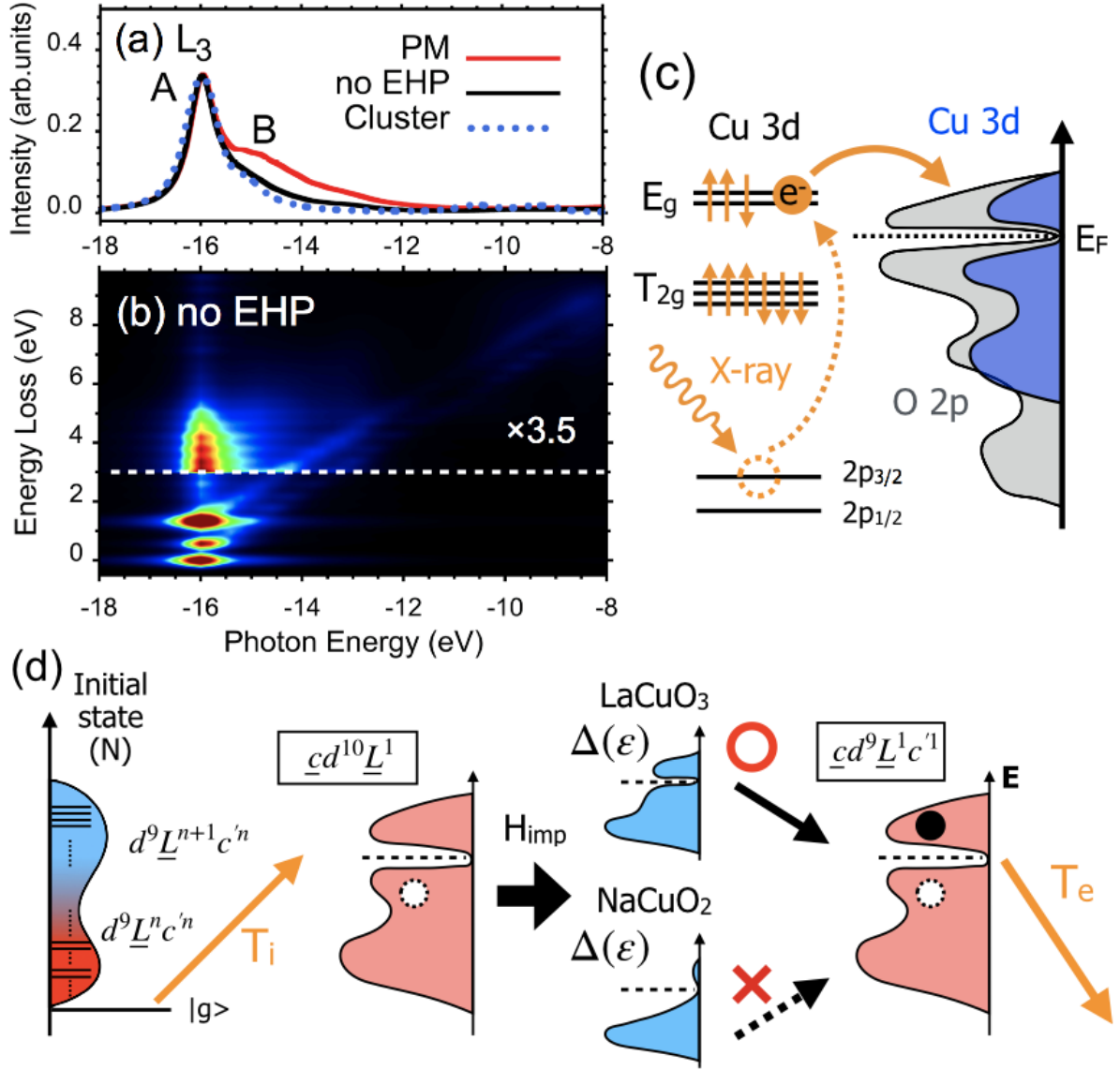
Figure 25: The calculated L-edge (a) XAS and (b) RIXS for $LaCuO_3$ in PM phase in which the CT to the conduction states above E_F is removed *only* in the intermediate state (denoted as 'no EHP'). (c) Schematic of CT to the conduction states in the intermediate state. (d) Schematic of electron-hole pair creation in RIXS process. Adapted from [15]

To confirm this interpretation, we 'switched off' the hybridization to the conduction band in the intermediate states for the PM phase of $LaCuO_3$, see Figs. 25(b,c). We set $\Delta(\varepsilon > 0) = 0$ in the H_{AIM} of Eq. 61 and kept the initial and final states corresponding to the unrestricted $\Delta(\varepsilon)$ unchanged. This suppresses the intensity of the FL feature. The RIXS spectra is similar to that of $NaCuO_2$ or the cluster model calculation. Final states with excited electron-hole pairs exist also in such a RIXS process, but they cannot be resonantly excited. The XAS spectra are also affected by switching off the hybridization

to the conduction states, see Fig. 25(a). The shoulder (B) is suppressed or in fact not existent, similar to the cluster model calculation. This confirms that intermediate states with localized and delocalized character coexist and thus FL and RL features can be observed in the RIXS spectra.

4.7 Conclusions

We studied within this thesis the coexistence of the RL and FL feature in two typical high valence cuprates. Only the RIXS spectrum of $LaCuO_3$ shows the FL feature, although a phase space for particle-hole excitations with mixed Cu $3d$ -O $2p$ exists in both cuprates. We showed that this is due to the different geometrical structure of $LaCuO_3$ and $NaCuO_2$. The unbound electron-hole excitations which are responsible for the FL feature cannot be excited by the RIXS process in $NaCuO_2$. This is captured by the hybridization function $\Delta(\varepsilon)$ of the AIM. Furthermore the low-ω_{loss} FL feature in $LaCuO_3$ is sensitive to a gap opening, which is also observed in experimental studies [17].

Reproducing qualitative and quantitative representative RIXS spectra with computational methods requires advanced many-body calculations. The many-body calculations can capture the FL and the RL behavior in the RIXS spectra simultaneously. The approach to combine the AIM with an LDA+DMFT bath was developed and applied to spectral calculations by Hariki et al. [22, 62]. The spectral calculations within our thesis reflect experimental studies [17] and the approach opened a window for further RIXS studies of various TM compounds.

References

[1] S. Maekawa, T. Tohyama, S.E. Barnes, S. Ishihara, W. Koshibae, and G. Khaliullin. Physics of Transition Metal Oxides. Springer Series in Solid-State Sciences. Springer Berlin Heidelberg, 2004.

[2] Masatoshi Imada, Atsushi Fujimori, and Yoshinori Tokura. Metal-insulator transitions. Rev. Mod. Phys., 70:1039–1263, Oct 1998.

[3] Daniel I. Khomskii. Transition Metal Compounds. Cambridge University Press, 2014.

[4] J. Kuneš, V. I. Anisimov, A. V. Lukoyanov, and D. Vollhardt. Local correlations and hole doping in nio: A dynamical mean-field study. Phys. Rev. B, 75:165115, Apr 2007.

[5] J. Kuneš, V. I. Anisimov, S. L. Skornyakov, A. V. Lukoyanov, and D. Vollhardt. Nio: Correlated band structure of a charge-transfer insulator. Phys. Rev. Lett., 99:156404, Oct 2007.

[6] G. A. Sawatzky and J. W. Allen. Magnitude and origin of the band gap in nio. Phys. Rev. Lett., 53:2339–2342, Dec 1984.

[7] K. Terakura, T. Oguchi, A. R. Williams, and J. Kübler. Band theory of insulating transition-metal monoxides: Band-structure calculations. Phys. Rev. B, 30:4734–4747, Oct 1984.

[8] Atsushi Hariki. New theoretical framework for core-level X-ray spectroscopy analysis based on dynamical mean-field theory and its application. PhD thesis, Osaka Prefecture University, January 2016.

[9] N F Mott. The basis of the electron theory of metals, with special reference to the transition metals. Proceedings of the Physical Society. Section A, 62(7):416, 1949.

[10] J. Zaanen, G. A. Sawatzky, and J. W. Allen. Band gaps and electronic structure of transition-metal compounds. Phys. Rev. Lett., 55:418–421, Jul 1985.

[11] D. Khomskii. Unusual valence, negative charge-transfer gaps and self-doping in transition-metal compounds. eprint arXiv:cond-mat/0101164, January 2001.

[12] Frank de Groot and A. Kotani. Core level spectroscopy of solids. Number v. 6 in Advances in condensed matter science. CRC Press, Boca Raton, 2008. OCLC: ocn156785114.

[13] S. Hüfner. Photoelectron spectroscopy: principles and applications. Springer Series in Solid-State Sciences Series. Springer-Verlag, 1996.

[14] F. M. F. de Groot, J. C. Fuggle, B. T. Thole, and G. A. Sawatzky. 2p x-ray absorption of 3d transition-metal compounds: An atomic multiplet description including the crystal field. Phys. Rev. B, 42:5459–5468, Sep 1990.

[15] A. Hariki, M. Winder, and J. Kuneš. Continuum charge excitations in high-valance transition metal oxides revealed by resonant inelastic X-ray scattering. ArXiv e-prints, March 2018.

[16] R. J. Green, M. W. Haverkort, and G. A. Sawatzky. Bond disproportionation and dynamical charge fluctuations in the perovskite rare-earth nickelates. Phys. Rev. B, 94:195127, Nov 2016.

[17] Valentina Bisogni, Sara Catalano, Robert J. Green, Marta Gibert, Raoul Scherwitzl, Yaobo Huang, Vladimir N. Strocov, Pavlo Zubko, Shadi Balandeh, Jean-Marc Triscone, George Sawatzky, and Thorsten Schmitt. Ground-state oxygen holes and the metal–insulator transition in the negative charge-transfer rare-earth nickelates. Nature Communications, 7:13017, October 2016.

[18] L. Chaix, G. Ghiringhelli, Y. Y. Peng, M. Hashimoto, B. Moritz, K. Kummer, N. B. Brookes, Y. He, S. Chen, S. Ishida, Y. Yoshida, H. Eisaki, M. Salluzzo, L. Braicovich, Z. X. Shen, T. P. Devereaux, and W. S. Lee. Dispersive charge density wave excitations in bi2sr2cacu2o8+δ. Nature Physics, 13:952 EP –, 06 2017.

[19] D. Betto, Y. Y. Peng, S. B. Porter, G. Berti, A. Calloni, G. Ghiringhelli, and N. B. Brookes. Three-dimensional dispersion of spin waves measured in nio by resonant inelastic x-ray scattering. Phys. Rev. B, 96:020409, Jul 2017.

[20] Ke-Jin Zhou, Milan Radovic, Justine Schlappa, Vladimir Strocov, Ruggero Frison, Joel Mesot, Luc Patthey, and Thorsten Schmitt. Localized and delocalized ti 3d carriers in laalo$_3$/srtio$_3$ superlattices revealed by resonant inelastic x-ray scattering. Phys. Rev. B, 83:201402, May 2011.

[21] F. Pfaff, H. Fujiwara, G. Berner, A. Yamasaki, H. Niwa, H. Kiuchi, A. Gloskovskii, W. Drube, J. Gabel, O. Kirilmaz, A. Sekiyama, J. Miyawaki, Y. Harada, S. Suga, M. Sing, and R. Claessen. Raman and fluorescence contributions to the resonant inelastic soft x-ray scattering on laalo$_3$/srtio$_3$ heterostructures. Phys. Rev. B, 97:035110, Jan 2018.

[22] Atsushi Hariki, Takayuki Uozumi, and Jan Kuneš. Lda+dmft approach to core-level spectroscopy: Application to 3d transition metal compounds. Phys. Rev. B, 96:045111, Jul 2017.

[23] Kozo Okada and Akio Kotani. Multiplet splitting in ni 2p x-ray photoemission spectra of ni dihalides. Journal of the Physical Society of Japan, 60(3):772–775, 1991.

[24] A. E. Bocquet, T. Mizokawa, T. Saitoh, H. Namatame, and A. Fujimori. Electronic structure of 3d-transition-metal compounds by analysis of the 2p core-level photoemission spectra. Phys. Rev. B, 46:3771–3784, Aug 1992.

[25] M. Taguchi, A. Chainani, K. Horiba, Y. Takata, M. Yabashi, K. Tamasaku, Y. Nishino, D. Miwa, T. Ishikawa, T. Takeuchi, K. Yamamoto, M. Matsunami, S. Shin, T. Yokoya, E. Ikenaga, K. Kobayashi, T. Mochiku, K. Hirata, J. Hori, K. Ishii, F. Nakamura, and T. Suzuki. Evidence for suppressed screening on the surface of high temperature $la_{2-x}sr_xcuo_4$ and $nd_{2-x}ce_xcuo_4$ superconductors. Phys. Rev. Lett., 95:177002, Oct 2005.

[26] M. Taguchi, M. Matsunami, Y. Ishida, R. Eguchi, A. Chainani, Y. Takata, M. Yabashi, K. Tamasaku, Y. Nishino, T. Ishikawa, Y. Senba, H. Ohashi, and S. Shin. Revisiting the valence-band and core-level photoemission spectra of nio. Phys. Rev. Lett., 100:206401, May 2008.

[27] M. Taguchi, A. Chainani, N. Kamakura, K. Horiba, Y. Takata, M. Yabashi, K. Tamasaku, Y. Nishino, D. Miwa, T. Ishikawa, S. Shin, E. Ikenaga, T. Yokoya, K. Kobayashi, T. Mochiku, K. Hirata, and K. Motoya. Bulk screening in core-level photoemission from mott-hubbard and charge-transfer systems. Phys. Rev. B, 71:155102, Apr 2005.

[28] R. Eguchi, M. Taguchi, M. Matsunami, K. Horiba, K. Yamamoto, A. Chainani, Y. Takata, M. Yabashi, D. Miwa, Y. Nishino, K. Tamasaku, T. Ishikawa, Y. Senba, H. Ohashi, I. H. Inoue, Y. Muraoka, Z. Hiroi, and S. Shin. Electronic structure of 3 d1 configuration vanadium oxides studied by soft x-ray and hard x-ray photoemission spectroscopy. Journal of Electron Spectroscopy and Related Phenomena, 156-158:421–425, 5 2007.

[29] R. Eguchi, M. Taguchi, M. Matsunami, K. Horiba, K. Yamamoto, Y. Ishida, A. Chainani, Y. Takata, M. Yabashi, D. Miwa, Y. Nishino, K. Tamasaku, T. Ishikawa, Y. Senba, H. Ohashi, Y. Muraoka, Z. Hiroi, and S. Shin. Photoemission evidence for a mott-hubbard metal-insulator transition in vo_2. Phys. Rev. B, 78:075115, Aug 2008.

[30] S Suga, A Sekiyama, S Imada, T Miyamachi, H Fujiwara, A Yamasaki, K Yoshimura, K Okada, M Yabashi, K Tamasaku, A Higashiya, and T Ishikawa. 8kev photoemission of the metal insulator transition system vo 2. New Journal of Physics, 11(10):103015, 2009.

[31] M. Obara, A. Sekiyama, S. Imada, J. Yamaguchi, T. Miyamachi, T. Balashov, W. Wulfhekel, M. Yabashi, K. Tamasaku, A. Higashiya, T. Ishikawa, K. Fujiwara, H. Takagi, and S. Suga. V-v dimerization effects on bulk-sensitive hard x-ray photoemission spectra for magneli phase vanadium oxides. Phys. Rev. B, 81:113107, Mar 2010.

[32] K. Horiba, M. Taguchi, A. Chainani, Y. Takata, E. Ikenaga, D. Miwa, Y. Nishino, K. Tamasaku, M. Awaji, A. Takeuchi, M. Yabashi, H. Namatame, M. Taniguchi, H. Kumigashira, M. Oshima, M. Lippmaa, M. Kawasaki, H. Koinuma, K. Kobayashi, T. Ishikawa, and S. Shin. Nature of the well screened state in hard x-ray mn $2p$ core-level photoemission measurements of $la_{1-x}sr_x mno_3$ films. Phys. Rev. Lett., 93:236401, Nov 2004.

[33] Hidekazu Tanaka, Yasutaka Takata, Koji Horiba, Munetaka Taguchi, Ashish Chainani, Shik Shin, Daigo Miwa, Kenji Tamasaku, Yoshinori Nishino, Tetsuya Ishikawa, Eiji Ikenaga, Mitsuhiro Awaji, Akihisa Takeuchi, Tomoji Kawai, and Keisuke Kobayashi. Electronic structure of strained $(la_{0.85}ba_{0.15})Mno_3$ thin films with room-temperature ferromagnetism investigated by hard x-ray photoemission spectroscopy. Phys. Rev. B, 73:094403, Mar 2006.

[34] S. Ueda, H. Tanaka, E. Ikenaga, J. J. Kim, T. Ishikawa, T. Kawai, and K. Kobayashi. Mn $2p$ core-level spectra of $la_{1-x}ba_x mno_3$ thin films using hard x-ray photoelectron spectroscopy: Relation between electronic and magnetic states. Phys. Rev. B, 80:092402, Sep 2009.

[35] K. Horiba, A. Maniwa, A. Chikamatsu, K. Yoshimatsu, H. Kumigashira, H. Wadati, A. Fujimori, S. Ueda, H. Yoshikawa, E. Ikenaga, J. J. Kim, K. Kobayashi, and M. Oshima. Pressure-induced change in the electronic structure of epitaxially strained $la_{1-x}sr_x mno_3$ thin films. Phys. Rev. B, 80:132406, Oct 2009.

[36] P. A. Bhobe, A. Chainani, M. Taguchi, T. Takeuchi, R. Eguchi, M. Matsunami, K. Ishizaka, Y. Takata, M. Oura, Y. Senba, H. Ohashi, Y. Nishino, M. Yabashi, K. Tamasaku, T. Ishikawa, K. Takenaka, H. Takagi, and S. Shin. Evidence for a correlated insulator to antiferromagnetic metal transition in crn. Phys. Rev. Lett., 104:236404, Jun 2010.

[37] M. Taguchi, A. Chainani, M. Matsunami, R. Eguchi, Y. Takata, M. Yabashi, K. Tamasaku, Y. Nishino, T. Ishikawa, S. Tsuda, S. Watanabe, C.-T. Chen, Y. Senba, H. Ohashi, K. Fujiwara, Y. Nakamura, H. Takagi, and S. Shin. Anomalous state sandwiched between fermi liquid and charge ordered mott-insulating phases of ti_4o_7. Phys. Rev. Lett., 104:106401, Mar 2010.

[38] M. Paul, A. Müller, A. Ruff, B. Schmid, G. Berner, M. Mertin, M. Sing, and R. Claessen. Probing the interface of fe_3o_4/GaAs thin films by hard x-ray photoelectron spectroscopy. Phys. Rev. B, 79:233101, Jun 2009.

[39] K. Bilewska, E. Wolna, M. Edely, P. Ruello, and J. Szade. Evidence of charge disproportionation on the nickel sublattice in $eunio_3$ thin films: X-ray photoemission studies. Phys. Rev. B, 82:165105, Oct 2010.

[40] P. W. Anderson. Localized magnetic states in metals. Phys. Rev., 124:41–53, Oct 1961.

[41] Akio Kotani and Yutaka Toyozawa. Photoelectron spectra of core electrons in metals with an incomplete shell. Journal of the Physical Society of Japan, 37(4):912–919, 1974.

[42] O. Gunnarsson and K. Schönhammer. Electron spectroscopies for ce compounds in the impurity model. Phys. Rev. B, 28:4315–4341, Oct 1983.

[43] Takayuki Uozumi, Kozo Okada, and Akio Kotani. Electronic structures of ti and v oxides: Calculation of valence photoemission and bremsstrahlung isochromat spectra. Journal of the Physical Society of Japan, 62(8):2595–2599, 1993.

[44] G. Kotliar, S. Y. Savrasov, K. Haule, V. S. Oudovenko, O. Parcollet, and C. A. Marianetti. Electronic structure calculations with dynamical mean-field theory. Rev. Mod. Phys., 78:865–951, Aug 2006.

[45] Antoine Georges, Gabriel Kotliar, Werner Krauth, and Marcelo J. Rozenberg. Dynamical mean-field theory of strongly correlated fermion systems and the limit of infinite dimensions. Rev. Mod. Phys., 68:13–125, Jan 1996.

[46] J. Kuneš, I. Leonov, P. Augustinský, V. Křápek, M. Kollar, and D. Vollhardt. Lda+dmft approach to ordering phenomena and the structural stability of correlated materials. The European Physical Journal Special Topics, 226(11):2641–2675, Jul 2017.

[47] Arash A. Mostofi, Jonathan R. Yates, Giovanni Pizzi, Young-Su Lee, Ivo Souza, David Vanderbilt, and Nicola Marzari. An updated version of wannier90: A tool for obtaining maximally-localised wannier functions. Comput. Phys. Commun., 185(8):2309 – 2310, 2014.

[48] Jan Kuneš, Ryotaro Arita, Philipp Wissgott, Alessandro Toschi, Hiroaki Ikeda, and Karsten Held. Wien2wannier: From linearized augmented plane waves to maximally localized wannier functions. Comput. Phys. Commun., 181(11):1888 – 1895, 2010.

[49] M. A. van Veenendaal and G. A. Sawatzky. Nonlocal screening effects in 2p x-ray photoemission spectroscopy core-level line shapes of transition metal compounds. Phys. Rev. Lett., 70:2459–2462, Apr 1993.

[50] E. Pavarini, E. Koch, A. Lichtenstein, and D. (Eds.) Vollhardt. The LDA+DMFT approach to strongly correlated materials, volume 1 of Schriften des Forschungszentrums Jülich : Modeling and Simulation. 2011. Record converted from VDB: 12.11.2012.

[51] P. Hohenberg and W. Kohn. Inhomogeneous electron gas. Phys. Rev., 136:B864–B871, Nov 1964.

[52] W. Kohn and L. J. Sham. Self-consistent equations including exchange and correlation effects. Phys. Rev., 140:A1133–A1138, Nov 1965.

[53] Pa Blaha, Ka Schwarz, Ga Madsen, Da Kvasnicka, and J Luitz. WIEN2k, An Augmented Plane Wave + Local Orbitals Program for Calculating Crystal Properties (Karlheinz Schwarz, Techn. Universitat Wien, Austria, 2001), ISBN 3-9501031-1-2.

[54] Nicola Marzari and David Vanderbilt. Maximally localized generalized wannier functions for composite energy bands. Phys. Rev. B, 56:12847–12865, Nov 1997.

[55] Wei Ku, H. Rosner, W. E. Pickett, and R. T. Scalettar. Insulating ferromagnetism in $la_4ba_2cu_2o_{10}$: An ab initio wannier function analysis. Phys. Rev. Lett., 89:167204, Sep 2002.

[56] Anton Kokalj. Computer graphics and graphical user interfaces as tools in simulations of matter at the atomic scale. Computational Materials Science, 28(2):155 – 168, 2003. Proceedings of the Symposium on Software Development for Process and Materials Design.

[57] Eva Pavarini, E Koch, Frithjof Anders, and and M. Jarrell (eds. Correlated Electrons: From Models to Materials. 09 2012.

[58] Alessandro Toschi. Strong Electronic Correlation in Dynamical Mean Field Theory and Beyond. habilitation, TU Wien, 2011.

[59] Philipp Werner, Armin Comanac, Luca de' Medici, Matthias Troyer, and Andrew J. Millis. Continuous-time solver for quantum impurity models. Phys. Rev. Lett., 97:076405, Aug 2006.

[60] Lewin Boehnke, Hartmut Hafermann, Michel Ferrero, Frank Lechermann, and Olivier Parcollet. Orthogonal polynomial representation of imaginary-time green's functions. Phys. Rev. B, 84:075145, Aug 2011.

[61] Hartmut Hafermann, Kelly R. Patton, and Philipp Werner. Improved estimators for the self-energy and vertex function in hybridization-expansion continuous-time quantum monte carlo simulations. Phys. Rev. B, 85:205106, May 2012.

[62] Atsushi Hariki, Akihiro Yamanaka, and Takayuki Uozumi. Theory of spin-state selective nonlocal screening in co 2p x-ray photoemission spectrum of lacoo3. Journal of the Physical Society of Japan, 84(7):073706, 2015.

[63] H. A. Kramers and W. Heisenberg. Über die streuung von strahlung durch atome. Zeitschrift für Physik, 31(1):681–708, Feb 1925.

[64] A. Amorese, N. Caroca-Canales, S. Seiro, C. Krellner, G. Ghiringhelli, N. B. Brookes, D. V. Vyalikh, C. Geibel, and K. Kummer. High-resolution resonant inelastic soft X-ray scattering as a probe of the crystal electrical field in lanthanides demonstrated for the case of CeRh2Si2. ArXiv e-prints, March 2018.

[65] T. Mizokawa, H. Namatame, A. Fujimori, K. Akeyama, H. Kondoh, H. Kuroda, and N. Kosugi. Origin of the band gap in the negative charge-transfer-energy compound nacuo₂. Phys. Rev. Lett., 67:1638–1641, Sep 1991.

[66] T. Mizokawa, A. Fujimori, H. Namatame, Y. Takeda, and M. Takano. Electronic structure of tetragonal lacuo₃ studied by photoemission and x-ray-absorption spectroscopy. Phys. Rev. B, 57:9550–9556, Apr 1998.

[67] M. T. Czyżyk and G. A. Sawatzky. Local-density functional and on-site correlations: The electronic structure of la₂cuo₄ and lacuo₃. Phys. Rev. B, 49:14211–14228, May 1994.

[68] T. Mizokawa, A. Fujimori, H. Namatame, K. Akeyama, and N. Kosugi. Electronic structure of the local-singlet insulator nacuo₂. Phys. Rev. B, 49:7193–7204, Mar 1994.

[69] J. F. Bringley, B. A. Scott, S. J. La Placa, T. R. McGuire, F. Mehran, M. W. McElfresh, and D. E. Cox. Structure and properties of the lacuo$_{3-\delta}$ perovskites. Phys. Rev. B, 47:15269–15275, Jun 1993.

[70] S. Darracq, S. Matar, and G. Demazeau. Correlations between the structural distortion of lacuo3 lattice and the resulting physical properties. Solid State Commun, 85(11):961 – 965, 1993.

[71] Koichi Momma and Fujio Izumi. VESTA3 for three-dimensional visualization of crystal, volumetric and morphology data. Journal of Applied Crystallography, 44(6):1272–1276, Dec 2011.

[72] Thomas Williams, Colin Kelley, and many others. Gnuplot 4.6: an interactive plotting program. http://gnuplot.sourceforge.net/, April 2013.

[73] Robert D. Cowan. The Theory of Atomic Structure and Spectra (Los Alamos Series in Basic and Applied Sciences). University of California Press, 1981.

[74] Jack Sugar. Potential-barrier effects in photoabsorption. ii. interpretation of photoabsorption resonances in lanthanide metals at the 4d-electron threshold. Phys. Rev. B, 5:1785–1792, Mar 1972.

[75] Masahiko Matsubara, Takayuki Uozumi, Akio Kotani, and Jean Claude Parlebas. Charge transfer excitation in resonant x-ray emission spectroscopy of nio. Journal of the Physical Society of Japan, 74(7):2052–2060, 2005.

[76] Vienna scientific cluster vsc3. http://vsc.ac.at/systems/vsc-3/. Accessed: 2018-06-20.

[77] David J. Singh. Electronic structure of nacuo₂. Phys. Rev. B, 49:1580–1585, Jan 1994.

[78] D. Choudhury, P. Rivero, D. Meyers, X. Liu, Y. Cao, S. Middey, M. J. Whitaker, S. Barraza-Lopez, J. W. Freeland, M. Greenblatt, and J. Chakhalian. Anomalous charge and negative-charge-transfer insulating state in cuprate chain compound kcuo$_2$. Phys. Rev. B, 92:201108, Nov 2015.

[79] Kozo Okada and Akio Kotani. Large-cluster effects on core-level photoabsorption spectrum of lacuo 3. J. Phys. Soc. Jpn, 68(2):666–673, 1999.

[80] P. Thakur, V. Bisogni, J. C. Cezar, N. B. Brookes, G. Ghiringhelli, S. Gautam, K. H. Chae, M. Subramanian, R. Jayavel, and K. Asokan. Electronic structure of cu-doped zno thin films by x-ray absorption, magnetic circular dichroism, and resonant inelastic x-ray scattering. J. Appl. Phys., 107(10):103915, 2010.

[81] D. Alders, L. H. Tjeng, F. C. Voogt, T. Hibma, G. A. Sawatzky, C. T. Chen, J. Vogel, M. Sacchi, and S. Iacobucci. Temperature and thickness dependence of magnetic moments in nio epitaxial films. Phys. Rev. B, 57:11623–11631, May 1998.

[82] D. D. Sarma, O. Strebel, C. T. Simmons, U. Neukirch, G. Kaindl, R. Hoppe, and H. P. Müller. Electronic structure of high-T_c superconductors from soft-x-ray absorption. Phys. Rev. B, 37:9784–9787, Jun 1988.

[83] G Ghiringhelli, M Matsubara, C Dallera, F Fracassi, R Gusmeroli, A Piazzalunga, A Tagliaferri, N B Brookes, A Kotani, and L Braicovich. Nio as a test case for high resolution resonant inelastic soft x-ray scattering. J. Phys. Condens. Matter., 17(35):5397, 2005.

List of Figures